Powder Spray Laser Additive Manufacturing of Zirconium

by

Arshad Harooni

A thesis
presented to the University of Waterloo
in fulfillment of the
thesis requirement for the degree of
Master of Applied Science
in
Mechanical Engineering

Waterloo, Ontario, Canada, 2016

AUTHOR'S DECLARATION

I hereby declare that I am the sole author of this thesis. This is a true copy of the thesis, including any required final revisions, as accepted by my examiners.

I understand that my thesis may be made electronically available to the public.

Arshad Harooni

Abstract

Zirconium is commonly used in nuclear, chemical processing and biomedical applications due to its low thermal neutron cross-section, relatively high corrosion resistance and great biocompatibility. Although it is an ideal candidate for laser cladding and Laser Additive Manufacturing (LAM), prior to this work very little research existed to prove that this was possible. This study used a Direct Energy Deposition (DED) method with localized shielding to successfully deposit commercially pure zirconium on zirconium alloy substrate. Effects of laser power, laser scan speed, laser spot size and powder feed rate were evaluated on deposition rate, dilution, geometrical circularity and presence of defects for single layer clads. Optimized parameters were used to deposit multilayer clads using recycled and as-received powder. Tempered as-received powder LAM deposits had higher ductility and Ultimate Tensile Strength (UTS) than commercially manufactured zirconium alloy. It is suggested that recycled powder deposits had reduced ductility due to presence of higher porosity and/or powder particles that were highly contaminated with atmospheric gases. These contaminated particles adhered poorly with the surrounding matrix and appeared as porosities during sample preparation and fracture testing. The optimized shielding gas nozzle design achieved levels of atmospheric contamination in LAM deposits comparable to conventionally manufactured zirconium alloys. Lack of adequate shielding resulted in changes in microstructure, microhardness, chemistry and appearance. Further optimization of shielding gas nozzle can allow in-situ repair of zirconium components and other reactive metals with just localized shielding.

Acknowledgements

- Mehrdad Iravani from University of Waterloo for discussion on nozzle design, help with microhardness testing and evaluating the future prospects of this work

- Nazmul Huda of University of Waterloo for help with tensile testing

- Atif Harooni for help with fabricating testing fixtures and nozzles, lab setup, optical microscopy and microhardness testing

Dedication

I dedicate this thesis to my parents, Alfia and Ghulam-Us-Saiyedain Harooni, whose encouragement and support allowed me to pursue graduate studies.

Table of Contents

List of Figures

List of Tables

Chapter 1– Introduction

The objective of this work was to prove the feasibility of laser cladding and Laser Additive Manufacturing (LAM) of zirconium. Additionally, the objective was also to develop a system that was capable of doing so with localized shielding instead of a glove box type enclosure. This work is significant because very little published research exists on laser cladding and LAM of zirconium. The work is also of importance because it opens up the possibility for in-situ repairs of highly reactive metals like zirconium.

The research was performed on a Computer Numerical Controlled (CNC) machine that oriented and moved a zirconium alloy substrate in a plane perpendicular to the laser beam. Zirconium powder was added to the melt pool which increased its volume and resulted in a clad. Stacking the clads on top of one another resulted in three dimensional (3D) structures. This type of system is commonly referred to as a Direct Energy Deposition (DED) system in the additive manufacturing industry (Dutta and Froes, 2014). Although the terms "clad", "deposit" and "deposition" have been used interchangeably in this work, "clad" refers exclusively to a single layer of deposition.

In general, equipment cost, restrictions and complexity have been a barrier in the widespread implementation of LAM technology. Although commercially available LAM systems provide excellent shielding to the deposition by operating in a glove box type enclosure, this setup restricts the size of the parts that can be manufactured. Commercially available DED systems often utilize coaxial nozzles that provide precise powder feed rate and are able to achieve consistent deposition properties in all horizontal direction of travel. However, these nozzles are bulky and have a relatively small range of working distance. This makes it difficult to use them for in-situ repair applications.

Zirconium and zirconium alloy parts are often used in nuclear, medical and chemical processing industries (AWS, 2012; Balla et al., 2009; Lustman and Kerze, 1955). Considering the low production volume, high value and complex designs often involved in many of these

1

applications, the LAM of zirconium is an attractive option. The LAM technology can also be used for part repair and coating application (Toyserkani et al., 2004). To the best of author's knowledge, little published research exists on depositing pure zirconium powder onto a zirconium alloy substrate. There has only been limited prior work on laser cladding of Zr powder on other alloys. Balla et al. (2009) and Baloyi et al. (2014) focused on depositing zirconium based coatings on titanium based alloys; Yue et al. (2012) deposited a pure zirconium coating on a AZ91D magnesium alloy; and Wu and Hong (2000) deposited zirconium onto an austenitic stainless steel substrate. None of these publications evaluate the use of zirconium or zirconium based alloys for LAM (i.e.: by depositing onto zirconium based material), and do not study the role of deposition parameters on clad quality.

The current research developed a concentric lateral nozzle that is able to deliver powder metal and localized shielding. The nozzle is smaller and several times less expensive than commercially available coaxial nozzle which opens up the possibility for in-situ repairs. The influence of lateral nozzle design and shielding gas flow rate is evaluated on deposit properties in terms of level of atmospheric contamination, appearance, hardness, microstructure and cross sectional geometry. Lessons learned from this undertaking can be applied to other materials that have atmospheric gas reactivity less than or equal to that of zirconium alloys. Once the nozzle was developed, it was used to deposit pure zirconium clads on a zirconium alloy substrates. Laser power, laser scan speed, laser spot size and powder feed rate were optimized by studying their effect on clad quality. The clad quality was assessed based on deposition rate, dilution, geometrical circularity and presence of defects. The optimized parameters were used to create multilayer deposits using recycled and as-received powder. The properties of the deposits were compared based on general appearance, microstructure, hardness profile, tensile properties and fracture analysis.

This thesis has been divided into eight chapters. Chapter 2 – Literature Review and Background, introduces readers to potential use for zirconium alloys, challenges associated with using zirconium alloys, commercially available LAM systems and brief metallurgy of

zirconium alloys. Chapter 3 – Experimental Methods, describes the setup used during the laser deposition experiments and the testing methods used to evaluate them. Chapter 4 – Lateral Nozzle Evaluation with Auxiliary Shielding Capabilities, discusses the influence of shielding efficiency on the deposit and what can be done to further improve it. Chapter 5 – Process Window Development for Laser Cladding, describes how laser processing parameters can influence the properties of the resulting clad. Chapter 6 – Comparing Mechanical Properties and Microstructure of Zirconium Deposit Fabricated Using Laser Additive Manufacturing, compares the mechanical and microstructural properties of as-received and recycled powder multi-layer deposits. Chapter 7 – Conclusion, concludes this work and Chapter 8 – Future Work, discusses the future prospects for this research.

Chapter 2[*] – Literature Review and Background

The purpose of this chapter is to discuss potential applications and challenges of LAM zirconium alloys. The purpose is also to compare the commercially available LAM technologies. Finally, this chapter also discusses the equilibrium and non-equilibrium phase transformations in common zirconium alloys and the effect of elemental additions.

2.1 Current and Future Applications for LAM Zirconium

The most obvious application for LAM zirconium components would be in nuclear, medical and chemical processing industry where low production volume, high value and complex design of parts makes this technology very attractive. According to Lustman and Kerze (1955), low neutron absorption cross section and high corrosion resistance of zirconium and its alloys make it ideal for nuclear industry. In a study to evaluate the use of zirconium components for hip and knee implants, Balla et al. (2009) reported them as being hypoallergenic, biocompatible and osteoconductive. The researchers found that oxidized zirconium provided an excellent site for the growth of human osteoblast cells and resulted in higher wear resistance than commercially pure titanium and zirconium. AWS (2012) mentions that zirconium and its alloys also find use in chemical processing industry for their high corrosion resistance to most acids, strong alkalis, salt solution and molten salts.

Another potential application for zirconium involves the production of metallic glass, creating custom alloys or Metal Matrix Composites (MMC). In a study to laser clad preplaced zirconium powder on an austenitic stainless steel substrate, Wu and Hong (2000) attributed the formation of metallic glass to the high glass forming ability of zirconium and the high cooling

---

[*] Parts of this section were published in a non-peer reviewed conference paper entitled "Comparison of Nozzle Gas Shielding Techniques for Laser Cladding of Zirconium" at International Congress on Applications of Lasers & Electro-Optics (ICALEO®). Parts of this section were also published in a paper entitled "Processing Window Development for Laser Cladding of Zirconium on Zirconium Alloy" in Journal of Materials Processing Technology

rates created by the laser. The clad showed a duplex microstructure with regions of austenite and metallic glass, and exhibited a hardness that was 1.8 to 2.6 times higher than the substrate. Monfared et al. (2013) found that zirconium based metallic glasses showed great biocompatibility and potential for use as biomedical devices. Arora et al. (2013) found that zirconium based metallic glass showed higher hardness and cavitation erosion resistance than a commonly used hydro-turbine steel. Since mixing the zirconium powder with other powders allows customization of the deposition's chemistry, it is possible to choose powder mixtures congenial for formation of metallic glass. Similarly, the DED system can be used to create custom alloys and MMC. Emamian (2011) was able to create a MMC with Fe matrix and TiC particle by using a powder mixture of iron, titanium and graphite. Since titanium and zirconium share very similar metallurgical properties, it is highly likely that zirconium based MMC can also be created. It follows that LAM can be used to not only clad conventional parts with metallic glass, custom alloy or MMC coatings but also to create 3D structures using these new generation of materials.

2.2 Zirconium's shortcomings

Although zirconium offers several highly desirable properties, it also has some shortcomings. NFPA (1996) emphasizes that zirconium fines and dust are highly combustible and care needs to be taken while handing them. Danielson et al. (2004) recommended using an active polishing method with a hydrofluoric acid solution to prepare zirconium samples for optical microscopy. This required careful metallography procedures and keen attention to safety. Bláhová et al. (2009) and AWS (2012) reported that zirconium and its alloys react very readily with atmospheric gases at temperatures above 427°C. Additionally, AWS (2012) reported that zirconium welds were also susceptible to iron and carbon contamination. It follows that cladding of zirconium would require thorough cleaning of substrate prior to cladding and ample inert gas shielding during cladding.

2.3 LAM: Current Technology

Frazier (2014) mentioned that Additive Manufacturing (AM) is favored over conventional machining when low production volume are required, material cost is high, the material or geometry of the part makes it difficult to machine and/or logistics costs are high. The use of laser as an energy source for AM offers numerous advantages over electric arcs generated during conventional arc welding. Toyserkani et al. (2004) mentioned that the laser is more uniform, repeatable, creates a smaller HAZ, minimizes dilution and reduces distortion. Compared to lasers, electron beam offer an even higher power density. Dutta and Froes (2014) mentioned that although commercially available electron beam AM systems create parts with lower residual stress that often do not need to be stress relived, they are more expensive than laser based AM systems because they have to operate in a vacuum chamber instead of an inert gas chamber. Since electron beams also generate X-rays, greater degree of safeguarding is also required to protect the operator. Currently, laser based AM system are more popular than electron beam AM systems.

Currently, two main types of commercially available systems that appear capable of zirconium LAM are DED and Powder Bed Fusion (PBF). As shown by the schematic in Fig. 2-1b, DED based LAM systems use a laser to create a melt pool on the surface of the substrate. The substrate is mounted on a CNC machine that orients it in the plane perpendicular to the laser and moves it along a predetermined path (Dutta and Froes, 2014). Wire or powder is added to the melt pool which results in an increase in volume and creates a single layer of clad. Stacking the clads on top of one another results in 3D geometry. As shown by Fig. 2-1, two main configuration of nozzles can be used with the DED system. The coaxial nozzle can only be used with powders and create a powder discharge profile that is symmetrical to the laser's axis. These nozzles are able to provide excellent shielding and precisely control the amount of powder reaching the melt pool. The axisymmetric nature of the powder profile allow these nozzles to have even deposition properties in all directions of travel (Toyserkani et al., 2004). The coaxial nozzles tend to be fairly complex which often makes them bulky and expensive.

They also have a small range of working distance. Lateral nozzles introduce powder or wire asymmetrically to the axis of the laser. Their design is much simpler which allows them to be relatively inexpensive and have a smaller profile. The smaller profile can make them more manageable for in-situ repair applications. The clads created by these nozzles result in varying properties depending on the direction of nozzle travel relative to the substrate. When powder is used, these nozzles have less control over the amount of powder reaching the melt pool. These nozzle are also not as proficient at shielding the melt pool. The author of this work used a modified lateral nozzle for their experiments. Contrary to the schematic, their system did not have a source of shielding gas that travelled symmetrically along the axis of the laser to protect it from powder particles. The system is described in more detail in Chapter 3.
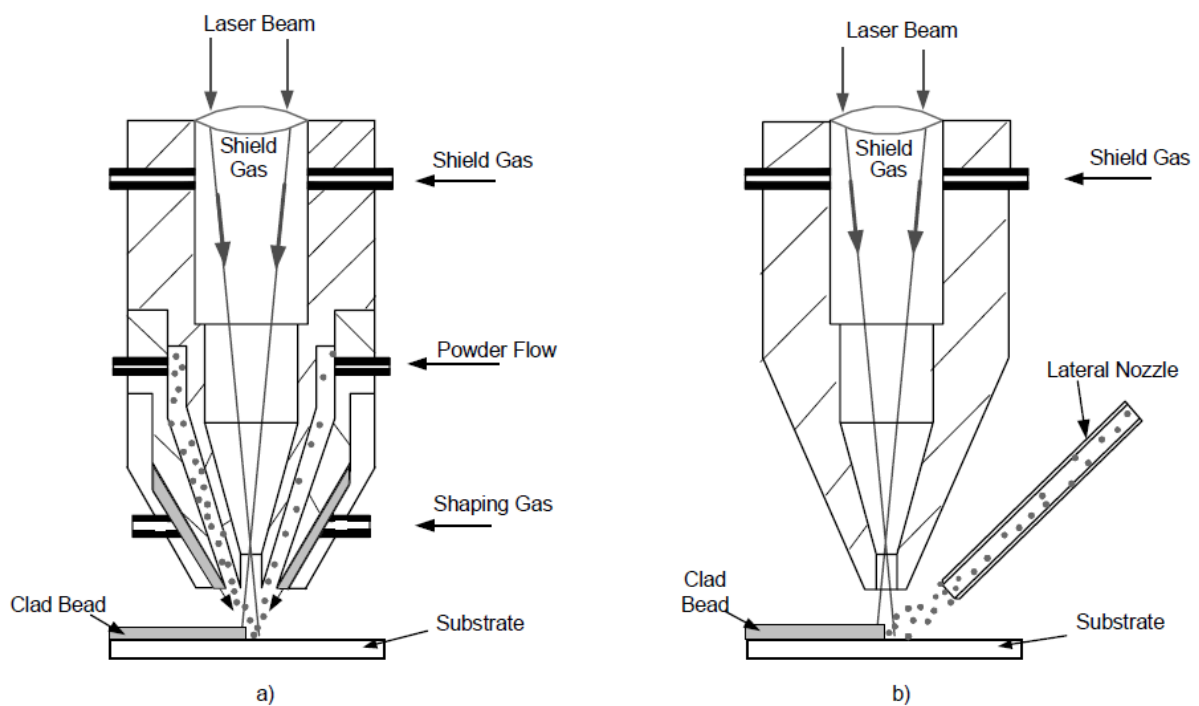
Figure 2-1 Direct Energy Deposition (DED) systems with **a:** coaxial nozzle; **b:** lateral Nozzle (Toyserkani et al., 2004)

As shown by Fig. 2-2, PBF based LAM systems operate by spreading a thin layer of powder on build plate. A laser selectively scans certain areas of the layer in predetermined pattern which melts the powder particles and allows them to fuse together when they solidify. Once a layer has been scanned, the build plate is lowered and a new layer of powder is spread on top. The process is repeated until the build is complete.
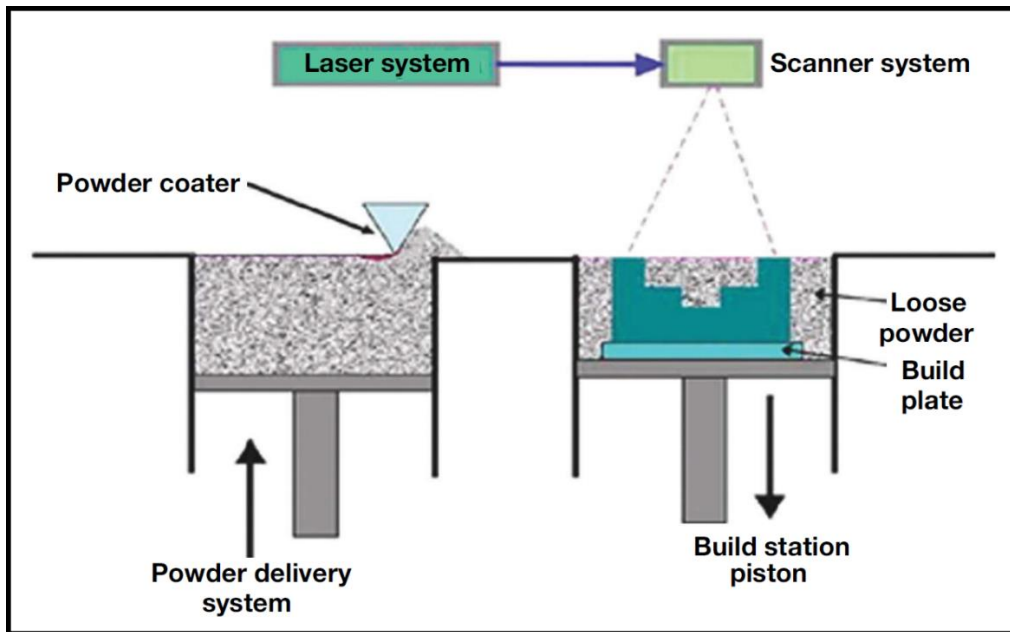
Figure 2-2 Powder Bed Fusion system (Dutta and Froes, 2014)

PBF, powder based DED and wire based DED technologies are compared in Table 2-1. Out of the three technologies, PBF is most proficient at creating complex geometrical features. The technology can also create hollow channels and unsupported structures (Dutta and Froes, 2014). The design of the PBF systems do not allow them to be used for building parts larger than the build station. This limits the size of the parts that can be built and prevents the technology from being used for in-situ repair applications. Since DED technology can operate with localized shielding, they can make parts bigger than their build station and also perform in-situ repairs. DED technology can achieve much higher deposition rates than PBF technology and are more suited for hard facing and repair applications (Dutta and Froes, 2014). Chapter 5

will show that porosity can be minimized in DED LAM by increasing the amount of energy used to deposit the material. Read et al. (2015) made a similar observation with PBF LAM of Al-Si-Mg alloy. Since DED systems typically use higher energy density, they are expected to have lower porosity than PBF systems. The advantage powder based DED system over other LAM systems is that it can be used for creating graded materials (Dutta and Froes, 2014). It is also very well suited for developing new alloys and MMC. Not all of the powder is utilized during PBF and powder based DED LAM systems. Wire based DED system can offer the lowest operational cost because they are able to deposit all of the wire during the LAM process. The cost of wire is also typically lower than powdered metal. Since powdered metal can create an explosive hazard, another major advantage of wire based DED systems is that they circumvent this hazard (Sciaky, 2015).

Table 2-1 Comparing commercially LAM technologies.

	PBF	Powder based DED	Wire based DED
Geometrical Accuracy	High (Dutta and Froes, 2014; Lumex Avance-25, 2014; Renishaw Canada, 2014; Sciaky, 2015)	Medium (Dutta and Froes, 2014; Joining Technologies, 2011; Sciaky, 2015)	Low (Dutta and Froes, 2014; Frazier, 2014)
Complexity of Parts	High (Dutta and Froes, 2014; Sciaky, 2015)	Low (Dutta and Froes, 2014; Sciaky, 2015)	Low (Dutta and Froes, 2014; Sciaky, 2015)
Deposition Rate	Low (Dutta and Froes, 2014; Sciaky, 2015; SLM Solutions NA, 2014)	Medium (Dutta and Froes, 2014; Fraunhofer IWS, 2011; Sciaky, 2015)	High (Fraunhofer IWS, 2011; Sciaky, 2015)
Chances of Porosity	High (Sciaky, 2015)	Low (Sciaky, 2015)	Low (Sciaky, 2015)
Creating gradient in material composition	Not Possible (Dutta and Froes, 2014)	Possible (Dutta and Froes, 2014)	Limited Possibility (Sciaky, 2015)
Hard facing and tool repair	Limited Possibility (Dutta and Froes, 2014)	Possible (Dutta and Froes, 2014)	Possible (Dutta and Froes, 2014)
In-situ repair	Not Possible (Dutta and Froes, 2014)	Possible (Dutta and Froes, 2014)	Possible (Dutta and Froes, 2014)
Consumable Waste	Medium	High (Sciaky, 2015)	Low (Sciaky, 2015)
Explosion and Health Hazard	High (NFPA, 1996; Sciaky, 2015)	High (NFPA, 1996; Sciaky, 2015)	Low (Sciaky, 2015)

Frazier (2014) noted that Ti-6Al-4V LAM parts with rougher surface finish than wrought alloys had poorer fatigue resistance. The surface roughness in the direction perpendicular to the energy source was 2-3 times higher than in the build direction. To mitigate the effects of surface roughness, most parts produced using LAM technologies require a finish machining operation (Dutta and Froes, 2014). This produces fatigue properties equivalent to wrought alloys (Frazier, 2014). As shown by Fig. 2-3, another method of minimizing surface roughness

is to use lower beam power to achieve better feature definition at the expense of lower build rates.
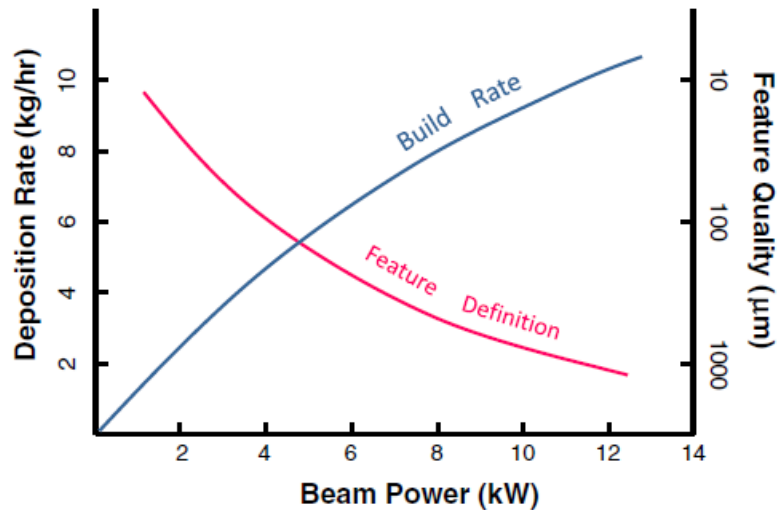
Figure 2-3 Relationship between deposition rate, beam power and feature quality (Frazier, 2014)

2.4 Metallurgy of Zirconium

2.4.1 Equilibrium Phase Transformations

Pure zirconium has a non-ideal Hexagonal Closed Packed (HCP) crystal structure at room temperature. This structure is known as the α phase. At around 862°C, α phase transforms into a Body Centered Cubic (BCC) crystal structure. This structure is known as the β phase. Pure zirconium melts at around 1852°C (Lustman and Kerze, 1955).

An ideal HCP crystal structure has a c/a ratio of 1.633 and has only 3 slip systems. An atom in this crystal structure will have 12 nearest equidistant neighbours (Campbell, 2008). At 20°C, pure zirconium has 6 nearest atoms at 3.1788 Å and another 6 second nearest atoms at 3.2311

Å. This brings the basal planes closer together and results in a c/a ratio of 1.593 (Lustman and Kerze, 1955). This in turn activates more than 3 slip systems and improves ductility. When pure zirconium transforms to β phase, 12 slip systems are activated, which is much more ductile than the α phase (Campbell, 2008).

There is a strong orientational relationship between the α and the β phase. When α phase transforms to β, the plane $\{0001\}_\alpha \parallel \{110\}_\beta$ and the direction $\langle 11\bar{2}0 \rangle_\alpha \parallel \langle 111 \rangle_\beta$ (Holt, 1970). It should be noted that the close packed planes of the HCP structure aligns itself with the closest packed plane of the BCC structure. The closest packed direction of the two crystal structure also align themselves. There is strong evidence to suggest that upon cooling from β phase, α nucleates as flat plates with $\left(10\bar{1}0\right)_\alpha$ faces precipitating on $\{112\}_\beta$ habit plane. The interface between these precipitates was observed to be coherent (Holt, 1970).

Crystalline structures tend to pack themselves as densely as possible because bonding energy is maximized when atoms are closely packed. Bonding energy is further increased when atoms have the greatest number of nearest neighboring atoms (Campbell, 2008). For this reason, zirconium's HCP α phase is ideal for maximizing bond energy at lower temperatures. There are two reasons to explain why zirconium transforms into a less dense BCC crystal structure at higher temperatures. The first reason is that even though the BCC atoms have only 8 nearest atoms, they have 6 second nearest atoms that are closer to it than the HCP structure. Energy calculations have indicated that the bonding energy of the second nearest atoms make a significant contribution to the overall bonding energy (Campbell, 2008). The second reason is that less dense structures allow the structure to sustain greater entropy and remain stable at higher temperatures (Campbell, 2008).

Zirconium experiences an apparent contraction in atomic size when it transforms from α to β phase. This phenomenon occurs in many crystal structures when they transform from a higher coordination number to a lower one (Lustman and Kerze, 1955). This general phenomenon is known as the Goldschmidt Contraction. Just before transitioning from α to β

phase at 862°C, zirconium has 6 nearest neighbours at 3.2083Å and 6 second nearest neighbours at 3.2505Å. After the transformation, zirconium has 8 nearest atoms at 3.1255Å. This phenomenon causes zirconium's volume to decrease when it transforms from α to β phase (Lustman and Kerze, 1955).

2.4.2 Non-Equilibrium Phase Transformations

Depending on the alloy composition and thermomechanical treatment, a number of non-equilibrium phases can exist at room temperatures in zirconium alloys. These include retained β phase, HCP martensitic α' phase, orthorhombic martensitic α'' phase and a hexagonal ω athermal phase (Sattari et al., 2013). Sattari et al. (2013) also pointed out stress as well as fast cooling rates can trigger the formation of athermal and martensitic phases in titanium and zirconium alloys. Table 2-3 summarizes some of the common phases that can be found at room temperature in zirconium alloys.

Table 2-2 Common phases in zirconium alloys

Phase	Structure	Diffusional
α	HCP	Yes
β	BCC	Yes
α'	HCP	No
α''	Orthorhombic	No
ω	Hexagonal	No

Although the ω phase transformation can also be classified as a "displacive", "diffusionless" or "military" transformation, it is not considered a martensitic phases. Unlike the martensitic phases, change in temperature is not required for its formation. This has been

13

proven by quenching alloys at ultra-high quench rates of ~11000 K/s. The complete reversibility of this phase also suggests that this phase is not influenced by temperature changes (Tewari et al., 2008). The typical morphology of the ω phase is also quite different than martensitic phase as it forms discrete particles with ellipsoidal or cuboidal shape. The size and spacing between the particles is about 2 to 10 nm. Fig. 2-4 shows a dark field micrograph of ω phase in a retained β matrix. ω phase can also be found in plate like morphology when the alloy is subjected to dynamic high pressure loading (Tewari et al., 2008). Bhadeshia (2011) imagined BCC β structure as a series of $\{111\}_\beta$ planes with a stacking sequence of …ABC, ABC, ABC …. During β to ω transformation, the B and C planes collapse but the A plane remains unaffected. This results in stacking sequence of …AB', AB', AB', … where the B' plane has twice the atomic density of A plane. This causes the final ω to assume a primitive hexagonal crystal structure with a c/a ratio of ~0.6 (Bhadeshia, 2011).
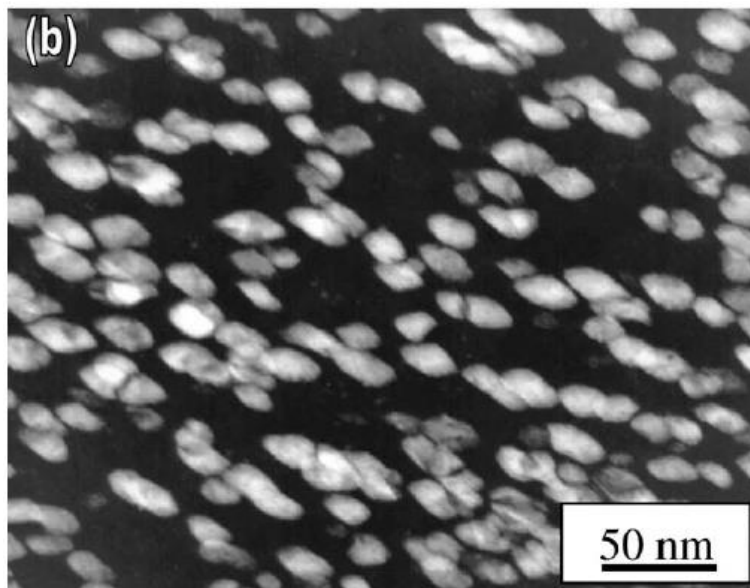
Figure 2-4 Dark-field micrograph of ω phase dispersed in retained β (Tewari et al., 2008)

Fig. 2-5 shows a pseudo-binary phase diagram of Zr-X alloys. The "X" in this diagram represents β stabilizing alloy. The α' and α'' martensitic start and finish lines have been

superimposed on this diagram. The start temperature for athermal ω phase has also been superimposed on this diagram (Sattari et al., 2013). For most β stabilized alloys, martensitic start (M_s) and martensitic finish (M_f) temperatures are separated by about 25°C. M_s and M_f temperatures lie in the α + β region of the alloy and decreases with increasing concentration of β stabilizing solute (Sattari et al., 2013). As shown by the diagram, when the β stabilizer concentration is very high, α', α'' and ω phase will not form. In this case, retained β will be the only non-equilibrium phase in the alloy. When there is an intermediate concentration on β stabilizers, ω will start to form in a retained β matrix. The transformation of β to ω will not finish. Further reducing the β stabilizer concentration will result in β transforming completely into α' and α'' martensite. A strong orientational relationship exists between the β and the other non-equilibrium phases (Sattari et al., 2013).
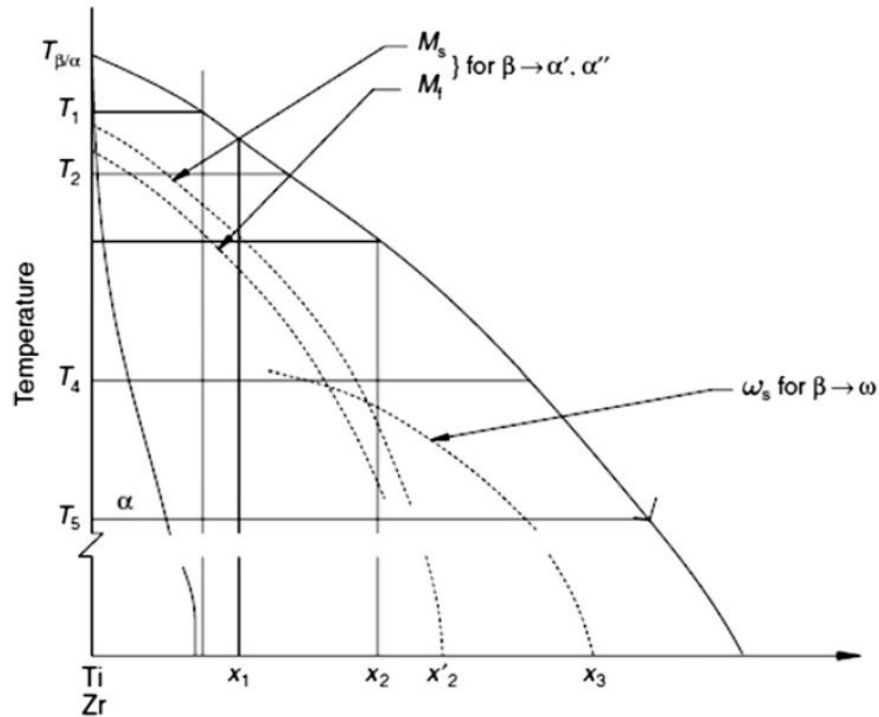
Figure 2-5 Pseudo-binary Zr-β stabilizer phase diagram with superimposed start and finish temperatures for non-equilibrium phases (Sattari et al., 2013).

As shown by Fig. 2-6, when the concentration of β stabilizers is high, only retained β is observed. At intermediate levels, lath shaped α'' martensitic phase is observed in a retained β matrix. At low levels, β phase transforms completely into acicular α' martensite (Sattari et al., 2013). Although not shown in this figure, α' martensite can also exist in a lath form. In the work done by Sattari et al. (2013), formation of α'' martensite required higher β stabilizer concentration than α' martensite. In their case, β phase was not able to completely transform into α'' martensite. Instead, the α'' martensitic phase existed with the athermal ω phase in a retained β matrix (Sattari et al., 2013).
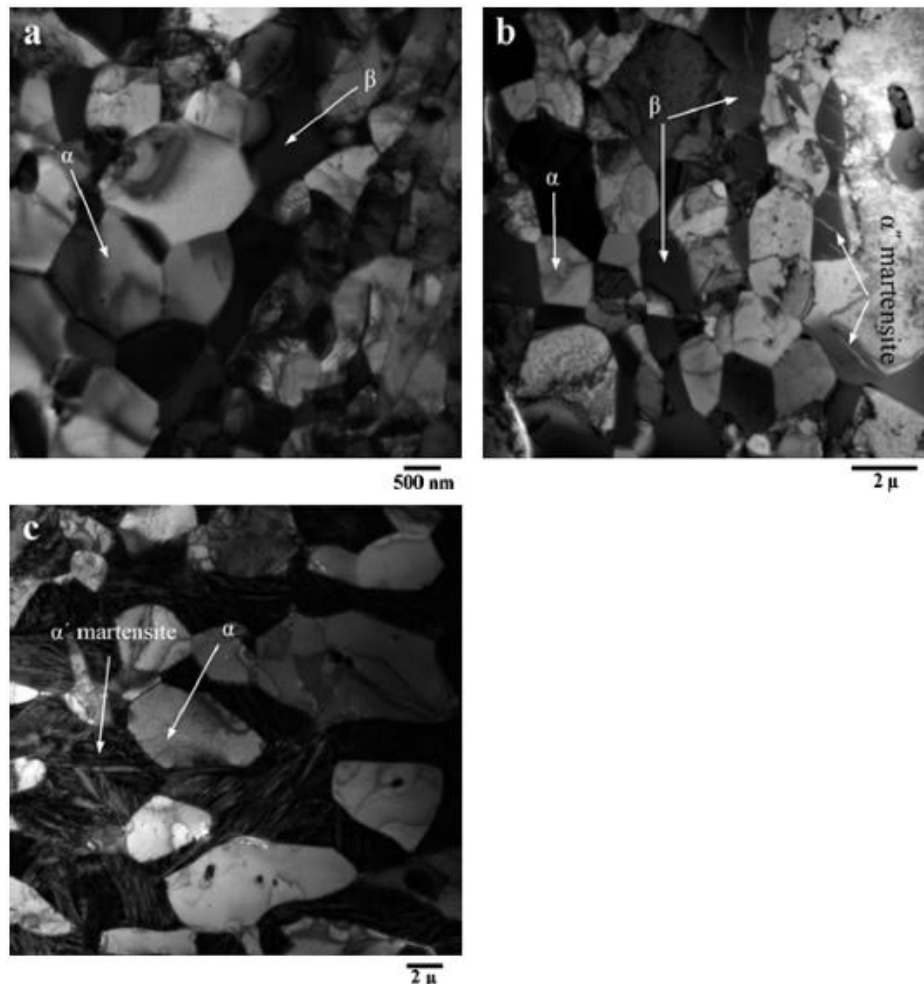
Figure 2-6 a) High; b) intermediate; c) low β stabilizer concentration in β phase (Sattari et al., 2013).

16

2.4.3 Alloying Elements in Zirconium Alloys

There are three main categories of zirconium alloys:

1. **Zirconium – tin alloys** (Brachet et al., 2011): These are alpha or near-alpha alloys (Campbell, 2008). Tin concentration in these alloys can range from ~1.0 to ~ 1.5 wt.% (Brachet et al., 2011). Zircaloy is an example of this alloy type. Although tin is the main alloying element, zircaloy also contains small amounts of iron, chromium and sometimes nickel (Campbell, 2008).

2. **Zirconium – Niobium alloys** (Brachet et al., 2011): These are alpha-beta alloys (Campbell, 2008). Niobium concentration ranges from ~1.0 to 2.5 wt. % (Brachet et al., 2011). An example of this type of alloys is Zr – 2.5 Nb. These alloys can be solution heat treated and aged to achieve strengths higher than zircaloy (Campbell, 2008).

3. **Quaternary Alloys** (Brachet et al., 2011): These are also alpha-beta alloys can be solution heat treated and aged (Campbell, 2008; Sattari et al., 2013). These alloys contain niobium and tin. They also contain either iron or molybdenum (Brachet et al., 2011; Sattari et al., 2013). The total alloying concentration is ~ 5.5 wt.%. These are newer generation of alloys and are showing potential to be used at higher operating temperatures than their predecessors. This can lead to higher thermal efficiencies in nuclear reactors. They have shown higher creep resistance and stress rupture properties than Zr-2.5Nb (Sattari et al., 2013).

Table 2-4 shows the effect of main alloying elements and common impurities on pure zirconium. Oxygen, nitrogen, hydrogen and carbon occupy interstitial spaces in the zirconium's crystal structure. The rest of the elements listed in Table 2-4 are substitutional alloying elements.

Table 2-3 Effect of commonly added substitutional alloying elements on zirconium (Brachet et al., 2011; Campbell, 2008; Lustman and Kerze, 1955; Nikulina and Malgin, 2008; Sattari et al., 2013)

Element	α - Stabilizer	β - Stabilizer	Effect of Alloying Element
Tin	X		• Solid Solution Strengthening • Low diffusion rate which results in low segregation • Segregation is further reduced with increase in O content • Increases fluidity of molten metal
Iron		X	• Provides Strengthening • Improves corrosion in water and steam
Molybdenum		X	• Very strong β stabilizer • Provides precipitation hardening potential
Niobium		X	• Similar effect as Molybdenum but to a lesser extent
Oxygen	X		• Up to 1500 wt. ppm added for interstitial (Octahedral) strengthening • Very high diffusion rate • Determines thickness of laths in α phase • Increases c and a parameter • c/a increases after 2.5 at.% O
Nitrogen	X		• Reduces corrosion resistance • Increases strength at the expense of ductility
Hydrogen		X	• Decreases fracture toughness
Carbon	Neutral		• Reduces corrosion resistance • Decreases fracture toughness • Promotes formation of Widmanstätten microstructural morphology in zircaloy

Chapter 3 – Experimental Methods†

This chapter (Harooni et al., 2015; Harooni et al., 2016) describes the equipment setup used during the experiments. It also specifies the sample preparation techniques and equipment used to characterize the resultant deposits.

In order to evaluate the role of LAM processing parameters during deposition of Zr powders, a standard operating procedure was first developed to maintain safe operation while handing the flammable powder. This required some precautions such as frequent cleaning to avoid accumulation of powder, and the addition of a tray to the deposition area to capture the non-adhered powder. Fig. 3-1a shows an isometric schematic of the experimental setup used during the laser cladding and LAM experiments. The substrate was mounted onto a copper backing, within a specially designed tray to capture excess powder. The tray was mounted on a CNC machine that allowed controlled motion in the plane perpendicular to the laser beam. The energy provided by the laser created a melt pool on the substrate. A lateral nozzle was used to deliver powder into the melt pool. The increase in volume of melt pool created by the additional powder resulted in the clad. Multilayer clad deposits were created by stacking these clads on top of one another.

---

† Parts of this section were published in a non-peer reviewed conference paper entitled "Comparison of Nozzle Gas Shielding Techniques for Laser Cladding of Zirconium" at International Congress on Applications of Lasers & Electro-Optics (ICALEO®). Parts of this section were also published in a paper entitled "Processing Window Development for Laser Cladding of Zirconium on Zirconium Alloy" in Journal of Materials Processing Technology

19
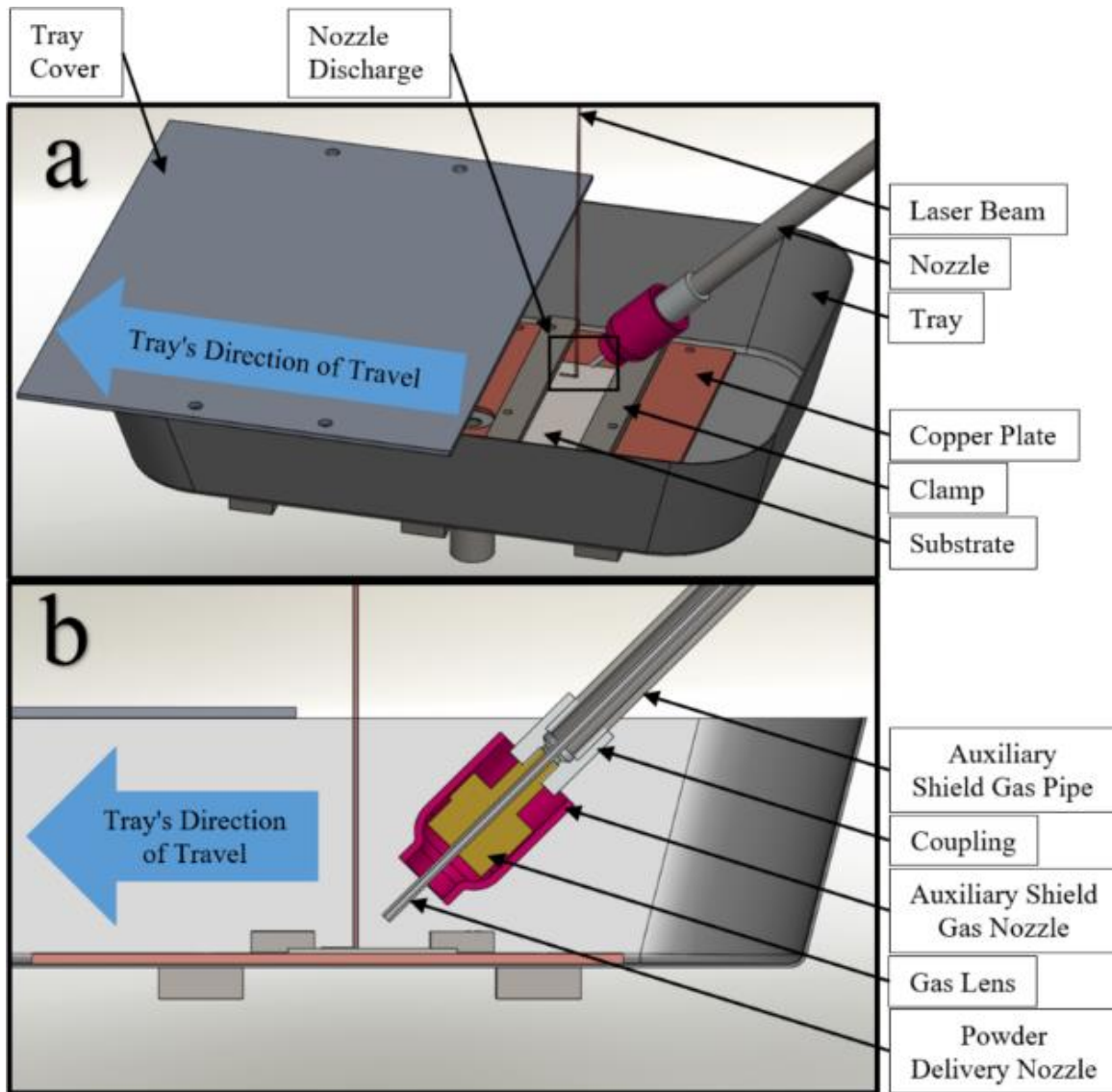
Figure 3-1 a: Isometric schematic of the setup used during experiments; **b:** Cross sectional view of the setup showing nozzle components

Sulzer Metco Twin-10-C gravity based powder feeder with metering wheel was employed. To send the powder through the powder delivery nozzle, an argon flow rate of 3.5 deciliter/min was used. A fiber laser (YLR-1000-IC by IPG Photonic), with a wavelength of 1070 nm, was used for the experiments. Motion was controlled by a Model 904-1 Fadal CNC machine.

Fig. 3-2 shows a close up of the discharge end of the nozzle. The nozzle was concentric; the inner nozzle delivered powder while the outer nozzle provided argon shielding. The inner powder delivery nozzle had a discharge diameter of 1.78 mm. Fig. 3-1b shows the nozzle configuration that was used for most of the experiments, where components of a TIG nozzle made up the outer nozzle. When a MIG nozzle was needed, the coupling, gas lens and the pink TIG nozzle cup were replace by a diffuser and a MIG nozzle.
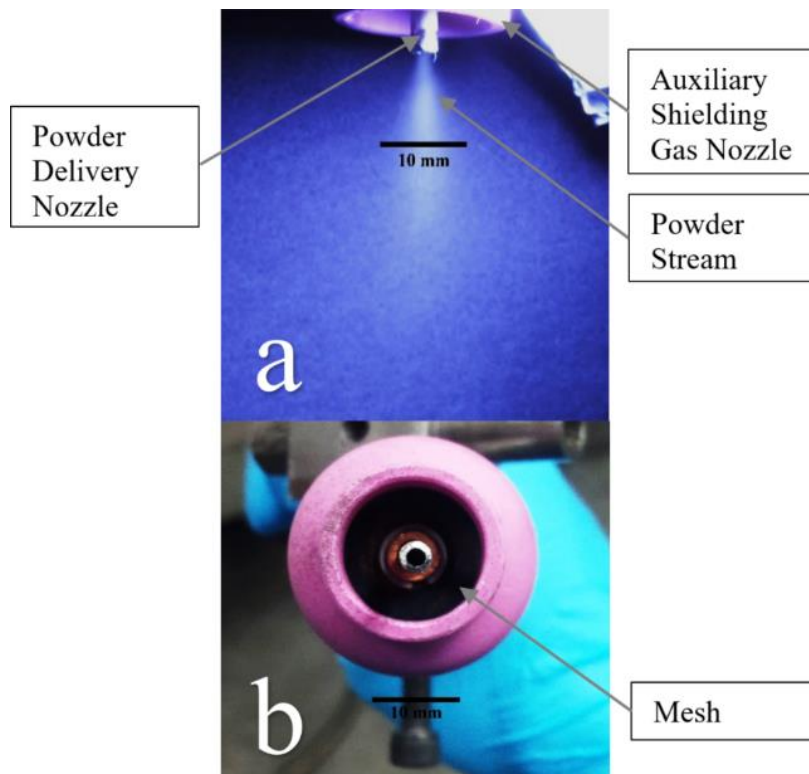
Figure 3-2 Nozzle discharge; **a:** Side view; **b:** Bottom view

Two very similar batches of spherical zirconium powder were used for the experiments. Table 3-1 and Table 3-2 show the chemical composition and size distribution of the second batch of as-received zirconium powder respectively. The substrate consisted of cold rolled sheets with dimension of 51 mm x 153 mm x 1.6 mm and with a measured composition of 97.10 wt. % Zirconium, 2.12 wt. % Niobium and 0.14 wt. % Tin. Abriata et al. (1986) reported

the melting point of pure zirconium to be 1855°C, while the phase diagrams presented by Lustman and Kerze (1955) indicates that the presence of niobium and tin will reduce this melting point by no more than 20°C. To prepare the sheets for laser cladding, they were cleaned with ethanol. Then, the side to be cladded was ground using 180 grit silicon carbide (SiC) paper until rolling marks from previous manufacturing process were no longer visible. The sheets were then cleaned with acetone and ethanol.

Table 3-1 Chemical composition of the second batch of powder

Element	Concentration (ppm)
C	70
Cr	<50
Fe	630
H	19
Hf	190
Mg	<1
N	270
Nb	<50
Ni	<35
O	2500
Si	17
Sn	335
Zr	9.96E+05

Table 3-2 Size distribution for the second batch of powder

Mesh size	Size Range (μm)	Weight Percent (%)
+120	>125	0.3
+140	105 to 125	3.3
+170	88 to 105	23.1
+200	74 to 88	34.4
+230	63 to 74	21.7
+270	53 to 63	9.1
+325	44 to 53	7.0
+400	37 to 44	0.5
+500	25 to 37	0.3
-500	<25	<0.1

Vickers hardness tests were performed using Nanovea® microindentation system. A 300 gram-force was used with a dwell time of 15 s. The system was set to have an approach speed of 30 μm/min when the sample was not in contact. The loading and unloading rates were set at 600 gram-force/min.

Electrical Discharge Machining (EDM) was used to prepare tensile coupons from multilayer clad deposits formed into freestanding wall structures. The process was used to remove asperities from the surfaces of the deposits to produce smooth edges. After x-ray radiography of the machined deposits, EDM was also used to machine the tensile coupons in accordance with Fig. 3-3. Tensile coupons from Zr-2.12Nb substrate were prepared using conventional machining in accordance with Fig. 3-4. The pin holes shown in Fig. 3-3 and Fig. 3-4 were enlarged to 3 mm using a conventional drill press. It is important to note that in order to maintain the miniature size of the tensile coupons, ASTM standards could not be followed. This means that elongation data in this work can only be compared to similar tensile coupons geometries. The tensile coupons were pulled at 0.5 mm/min and the engineering strain along the gauge thickness – gauge length plane was recorded using a Digital Image Correlation (DIC)

system. The cameras used for the system had a resolution of 5.0 Megapixels. The software used for the analysis was called Vic-3D and was created by Correlated Solutions Inc. A virtual linear extensometer was used and a subset size of 21 was used to analyze the data. The spacing between the two measuring points of the extensometer was not recorded during the testing. While setting up the tensile tester, the coupons were loaded into a set of tapered jaws by only the pins. The jaws tightened automatically during the early stages of the tensile test.
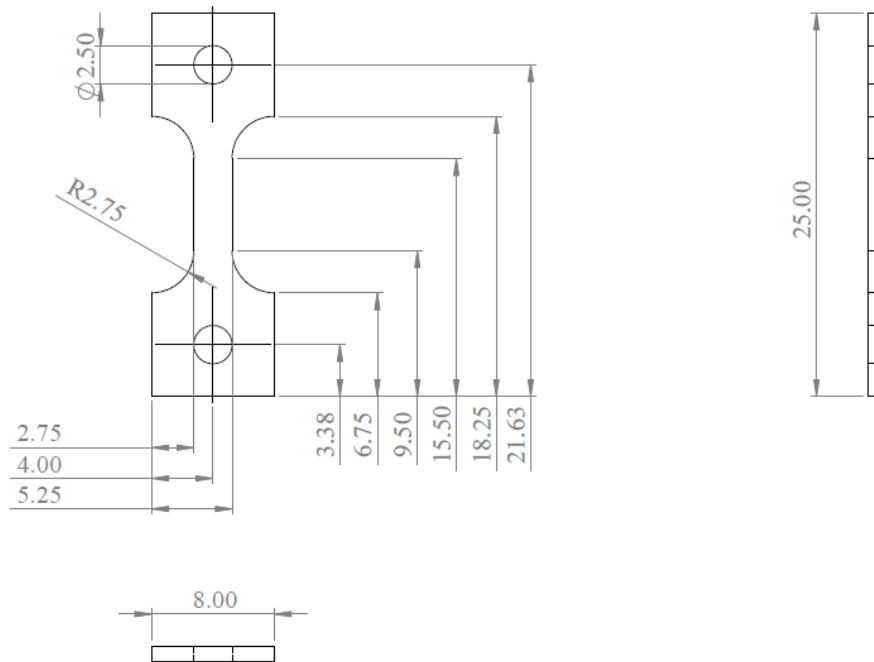
Figure 3-3 EDM geometry of coupons produced using multilayer clad deposits
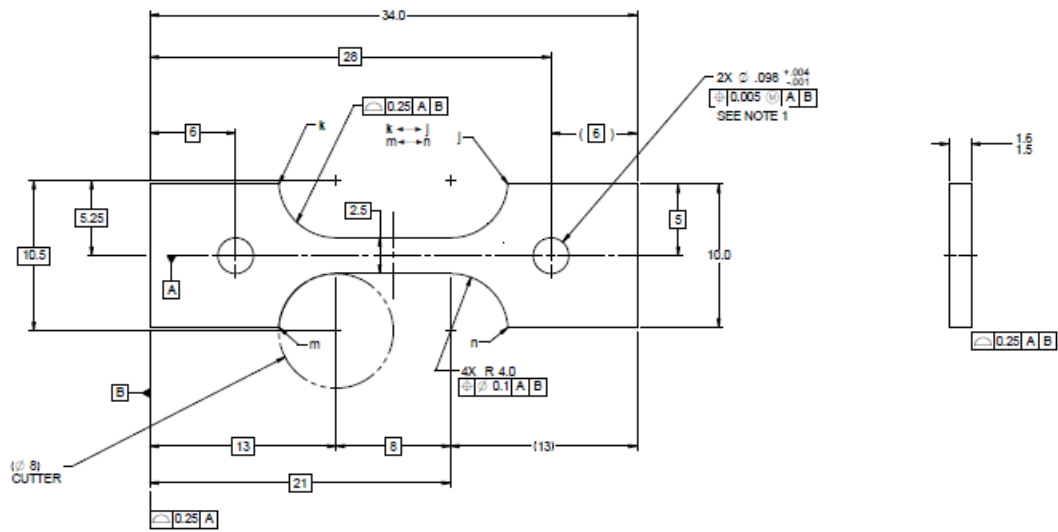
Figure 3-4 Conventionally machined geometry of coupons produced using Zr-2.12Nb substrate

To prepare the samples for optical microscopy, the deposition had to be active polished using a solution of 1 vol. % hydrofluoric acid, 3.5 vol. % nitric acid, 1.5 vol. % hydrogen peroxide and balance water. Extra care was taken to safeguard the researchers and properly dispose of the waste that resulted from sample preparation.

Chapter 4 – Lateral Nozzle Evaluation with Auxiliary Shielding Capability[‡]

This chapter (Harooni et al., 2015; Harooni et al., 2016) discusses the influence of shielding efficiency on the resultant deposit. The deposits were evaluated for their appearance, chemical composition, deposition properties, hardness and microstructure. The outcome of this chapter resulted in a powder delivery and shielding gas nozzle that was able to successfully deposit highly reactive zirconium powder with localized shielding instead of a glove box type environment. With further optimization, the results from this chapter could help create in-situ repair systems for zirconium and other reactive metals.

Bláhová et al. (2009) have noted that zirconium and its alloys react very readily with atmospheric gases at high temperatures. The purpose of this chapter is to establish the effect that atmospheric gases have on the properties of zirconium clads and find solutions to mitigate them. The following processing parameters were controlled in this chapter:

- Laser spot diameter = 1.4 mm
- Argon gas purity $\geq$ 99.995%
- Angle of nozzle to substrate = $40 \pm 5°$
- Distance from the powder delivery nozzle to the deposit = 8 mm to 12 mm

4.1 Nozzle Design

When Zr-alloys are heated above $427°C$ in an atmosphere that has unacceptable amount of air, the surface turns from silver to straw/gold, to purple, to light blue, to dark blue, to yellow, to dull grey, and finally to a powdery white/yellow as progressively increasing amount of atmospheric gases react with the surface. The discolouration of the resultant clads and their

---

[‡] Parts of this section were published in a non-peer reviewed conference paper entitled "Comparison of Nozzle Gas Shielding Techniques for Laser Cladding of Zirconium" at International Congress on Applications of Lasers & Electro-Optics (ICALEO®). Parts of this section were also published in a paper entitled "Processing Window Development for Laser Cladding of Zirconium on Zirconium Alloy" in Journal of Materials Processing Technology

surrounding area can be used to estimate the level of atmospheric contamination. An acceptable zirconium alloy weld can only have silver and dark straw colours (AWS, 2012). Fig. 4-1 shows that the nozzle used for Tungsten Inert Gas (TIG) welding is more effective at shielding clad surface than Metal Inert Gas (MIG) welding nozzle.
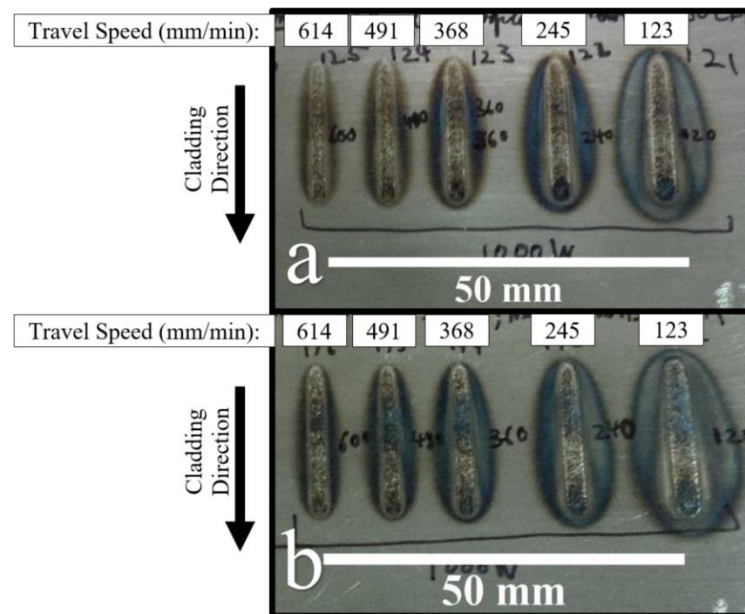
Figure 4-1 Effect of nozzle design on cladding appearance. **a:** TIG nozzle; **b:** MIG nozzle. The parameters used were: Laser power = 1000 W; Powder feed rate = 2.0 g/min; Auxiliary shielding gas inner diameter = 15.9 mm; Auxiliary shielding gas flow rate = 14.1 L/min; Powder condition = as-received;

According to Johnson et al. (2006), the shielding gas flow developing out of welding nozzles are especially complex because they have a relatively short distance to develop before they reach the substrate and have internal features that disrupt the flow's formation. The author identified that the ability of the shielding gas to displace atmospheric gases from the melt pool area was dependant on the nozzle design, distance of the nozzle to the workpiece, nozzle travel speed, discharge diameter of the nozzle, shielding gas flow rate, shielding gas purity and side winds. Zschetzsche (2012) showed that the arc drew the shielding gas towards the center of

the melt pool and resulted in better shielding. The author also found that nozzle orientation had an influence on melt pool shielding. For MIG nozzles, Zschetzsche (2012) observed that boreholes and other internal design features strongly influenced the flow that developed out of the nozzle. Increase in turbulence and flow separation at the substrate was observed as the shielding gas flow rate was increased for MIG (Johnson et al., 2006) and TIG (Siewert et al., 2014) nozzles. Although the turbulence is undesirable because it can result in greater mixing with atmospheric gases, operating at lower flow rates is not always an option because a minimum flow rate is required to overcome the diffusive and thermal buoyance effect (Siewert et al., 2014).

Fig. 4-2 show visualization of flows originating from MIG and TIG nozzles. Fig. 4-2a shows that laminar jets can be created out of TIG nozzles when a gas lens is used. Fig. 4-2b uses Schlieren technique which shows differences in densities of transparent media caused by mixing of different gases and gradients of pressure and temperature (Zschetzsche, 2012). The image shows a laminar jet of Argon forming over the substrate and displacing the atmospheric gases. Fig. 4-2c shows that although the MIG nozzle's impinging jet successfully displaces the air close to the electrode, flow separation on the substrate occurs a short radial distance away.
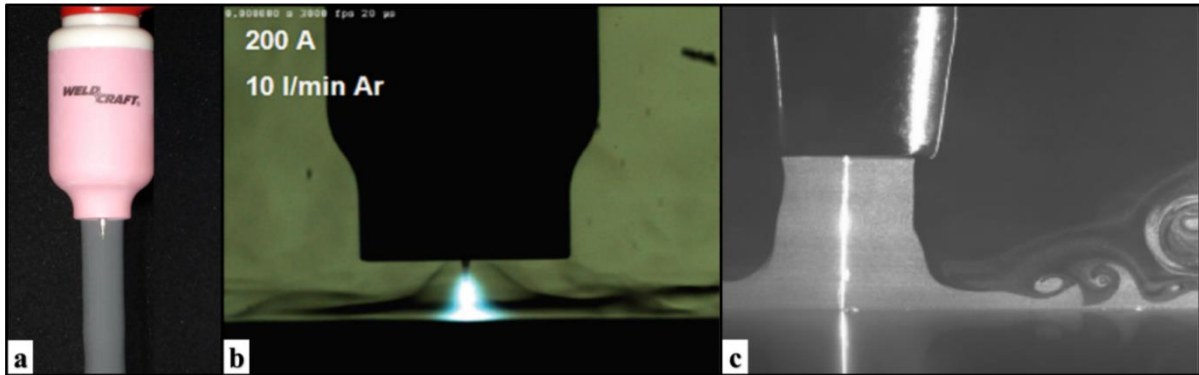
Figure 4-2 Visualization of flow developing out of welding nozzles. **a:** Seeded air creating a laminar jet out of a TIG nozzle at an unknown flow rate (Weldcraft, 2016); **b:** Schlieren technique showing argon gas from a TIG nozzle at 10 L/min displacing atmospheric gases (Siewert et al., 2014); **c:** Seeded air at 14.1 L/min out of a MIG nozzle creating an impinging jet (Johnson et al., 2006)

Due to the complexity of the flow that develops out of the welding nozzles, it is difficult to explain the difference in performance of TIG and MIG nozzles. However, it is suspected that the difference arises because MIG nozzles create more annular flow while the TIG nozzles create a more cylindrical flow. Johnson et al. (2006) found that increasing the stickout of the MIG nozzle's contact tip made the flow more annular and created more velocity fluctuation at the workpiece. Since the TIG nozzles' gas lens used for this chapter do not impede the gas flow to the same extent, their impinging flows are expected to be more cylindrical and cause smaller velocity fluctuations at the workpiece.

4.2 Other Laser Processing Parameters

Apart from the type of nozzle used, other factors that are expected to influence the shielding efficiency are: powder feed rate, interaction time, power density, projection area and shielding density. Clads in Fig. 4-1a were produced using a powder feed rate of 2.0g/min while clads in Fig. 4-3b were produced using a powder feed rate of 4.0g/min. Although the other

processing parameters were kept constant, it can be observed that clads in Fig.4-3b were less discoloured. This shows that increasing the powder feed rate improves the shielding efficiency, because it allows the atmospheric contaminants to dissolve within a larger clad.
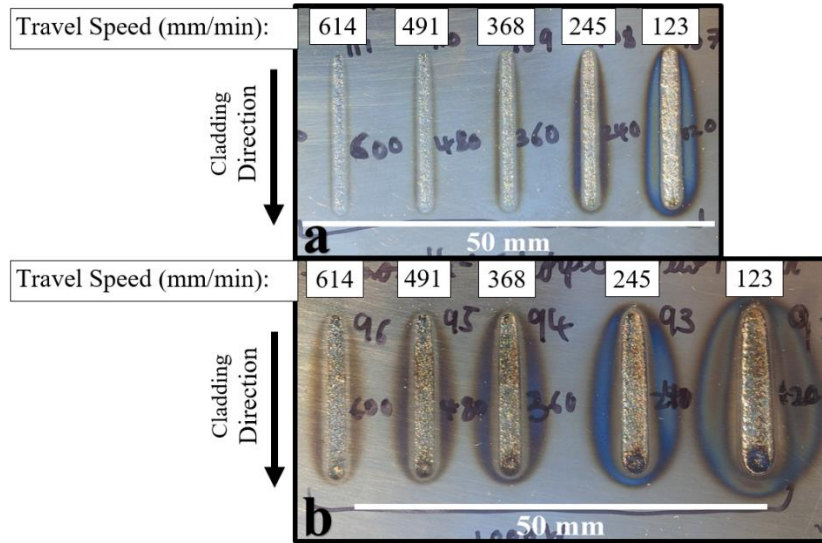
Figure 4-3 Effect of laser power and laser scan speed on cladding appearance. **a:** 400W; **b:** 1000W. The parameters used were: Powder feed rate = 4.0 g/min; Auxiliary shielding gas inner diameter = 15.9 mm; Auxiliary shielding gas flow rate = 14.1 L/min; Powder condition = as-received; Auxiliary shielding gas nozzle type = TIG

Steen et al. (2010) defined Interaction time and power density as:

$$Interaction\ time = \frac{\phi}{v} \qquad \text{(eq. 4-1)}$$

$$Power\ Density = \frac{4P}{\pi\phi^2} \qquad \text{(eq. 4-2)}$$

where ϕ is the laser spot diameter, v is the laser scan speed and P is the laser power.

Eq. 4-1 indicates that as the laser scan speed decreases, the interaction time increases. Similarly, Eq. 4-2 shows that increasing the laser power increases the power density. It can be observed from Fig. 4-3 that as the interaction time and power density increases, the discolouration in the clad and its surrounding area also increases. This indicates that more shielding is required for higher energy input clads. It is important to note from Fig. 4-3 that although the substrate surrounding the clad have an unacceptable level of discolouration, the clads themselves appear to be adequately protected based on the silver and straw coloured surface appearance.

In order to further analyze the laser clad characteristics, some other features need to be defined. The projection area, $\hat{A}$, is the discharge area of the auxiliary shielding gas nozzle when it is projected on the substrate and can be defined as:

$$\hat{A} = \frac{\pi D^2}{4 \sin \theta} \qquad \text{(eq. 4-3)}$$

where D is the inner diameter (ID) of the nozzle and θ is the angle of the nozzle relative to the substrate.

Shielding density, S, is a measure of how effective the shielding gas flow rate is for a particular nozzle diameter. Higher shielding density indicates a better ability to provide shielding. It can be defined as:

$$S = \frac{\dot{V}}{\hat{A}} \qquad \text{(eq. 4-4)}$$

where $\dot{V}$ is the auxiliary shielding gas flow rate.

Eq. 4-3 and 4-4 show that the shielding density decreases as the projection area increases for a particular auxiliary shielding gas flow rate. Fig. 4-4a shows that when the largest

diameter nozzle was used, the clad discolouration was the most consistent across the length of the clad line. This is due to the large projection area of the nozzle which allowed it to shield the entire length of the clad. The smallest nozzle had the highest shielding density but the lowest projection area. As shown in Fig. 4-4c, this resulted in very good shielding at the end of the clad but poor shielding for the rest of the clad. The auxiliary shielding gas nozzle with an ID of 15.9 mm provides a good compromise between projection area and shielding density. Fig. 4-4 also shows that the discolouration of the clad decreases as the auxiliary shielding gas flow rate increases for each nozzle design. Further improvement in shielding can likely be achieved by increasing the shielding density of the 15.9 mm ID nozzle. To achieve this, more than one welding flowmeter will be necessary because conventional welding flowmeters do not allow flow rates much higher than 33.0L/min.
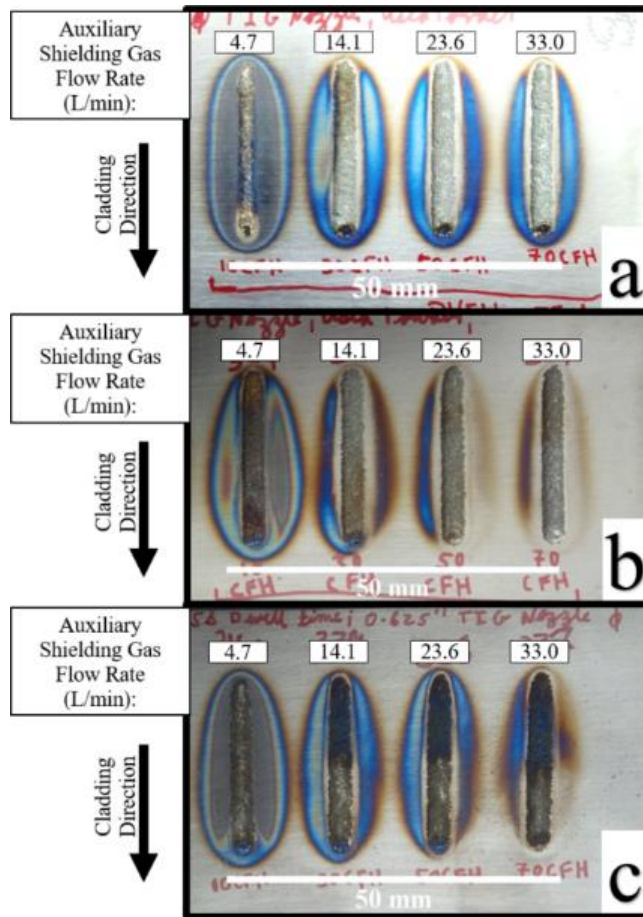
Figure 4-4 Effect of auxiliary shielding gas nozzle inner diameter and shielding gas flow rate on clad appearance. **a:** Diameter =28.6 mm; **b:** Diameter = 15.9 mm; **c:** Diameter =9.53 mm. The parameters used were: Laser power = 800 W; Laser scan speed = 245 mm/min; Powder feed rate = 8.9 g/min; Powder condition = recycled; Auxiliary shielding gas nozzle type = TIG

In order to assess the contamination levels within the clad deposits, Inductively Coupled Plasma (ICP) spectroscopy was performed to measure the resulting chemical composition. To prepare a sample, 10 clads were deposited on top of one another to build a small wall. The wall was drilled to extract chips for chemical analysis by ICP spectroscopy. The spectroscopy results were compared to the as-received powder and the results are listed in Table 4-1. The results indicate that the oxygen content of the clad produced with 14.1 L/min

33

of auxiliary shielding gas is only 300 ppm higher than the initial powder. According to the AWS (2012), 100-300 ppm of oxygen pickup during adequately shielded TIG welding of zirconium is quite typical. The results also show that increasing the shielding gas flow rate was successful in decreasing the oxygen and nitrogen contamination of the clads. The slight increase in the niobium content of the cladding would originate from the dilution with the substrate which had niobium content of 2.12%.

Table 4-1 Chemical composition of 10 layered clad deposited at varying shielding gas flow rate. The parameters used to during deposition were: Laser power = 800 W; Laser scan speed = 123 mm/min; Powder feed rate = 4.0 g/min; Powder condition = as-received; Auxiliary shielding gas nozzle type = TIG; Nozzle inner diameter = 15.9 mm

Component (ppm)	Shielding gas flow rate			As-received Powder
	4.7 L/min	9.4 L/min	14.1 L/min	
Fe	570	590	600	780
Hf	190	225	240	125
N	2800	670	410	360
Nb	4080	650	760	50
O	4900	2800	2800	2500
Si	19	18	17	14
Sn	260	295	290	425

Fig. 4-5 shows the influence of auxiliary shielding gas flow rate on the fusion area of the clad. The clad fusion area was observed to increase with increasing auxiliary shielding gas flow rate. This suggests that an oxide layer might be forming on the surface of the melt pool during laser cladding and inhibiting the powder from mixing with the melt pool. When less shielding is provided, a thicker and more uniform oxide layer may form and limit the mixing and deposition of incoming powder.
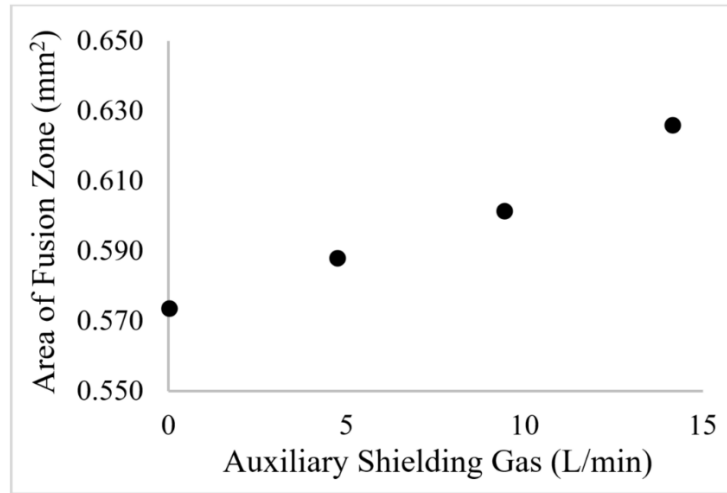
Figure 4-5 Fusion zone and shielding gas flow rate. The parameters used were: Laser power = 600 W; Laser scan speed = 123 mm/min; Powder feed rate = 4.0 g/min; Powder condition = as-received; Auxiliary shielding gas nozzle type = TIG; Nozzle inner diameter = 15.9 mm

The resulting contamination also has a significant effect on the hardness of the zirconium clads, since oxygen and nitrogen have an interstitial solid solution strengthening effect. The manifestation of this effect can be observed in Fig. 4-7, where hardness is observed to increase with increasing atmospheric contamination that occurs with lower shielding gas flow rates.
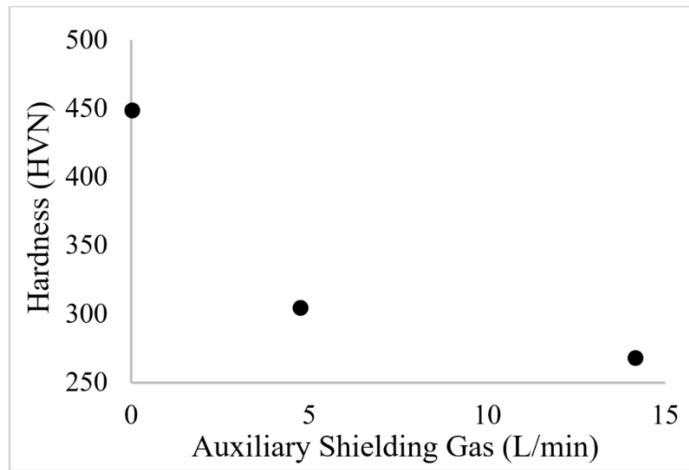
Figure 4-6 Hardness and shielding gas flow rate. The parameters used were: Laser power = 600 W; Laser scan speed = 123 mm/min; Powder feed rate = 4.0 g/min; Powder condition = as-received; Auxiliary shielding gas nozzle type = TIG; Nozzle inner diameter = 15.9 mm

The presence of atmospheric contamination also has a dramatic influence on the microstructures produced. Since nitrogen and oxygen are both strong αZr stabilizers (Abriata et al., 1986; Gribaudo et al., 1994; Lustman and Kerze, 1955), the presence of these contaminants has a significant impact on the resulting microstructures. As shown in Fig. 4-7, when no auxiliary shielding gas is used during deposition, the clads consisted of a feathery coarse Widmanstätten microstructure. In contrast, when ample auxiliary shielding is used, the clads consisted of an ultra-fine martensitic structure with interlocking needles, see Fig. 4-8. Although the microstructure shown in Fig. 4-7 was much larger than Fig. 4-8, its hardness was higher due to the drastically higher contribution of solid solution strengthening by the oxygen and nitrogen. It is generally desired to avoid excessively hard and strengthened zirconium alloy properties in order to avoid embrittlement of the material in most applications requiring good mechanical performance.
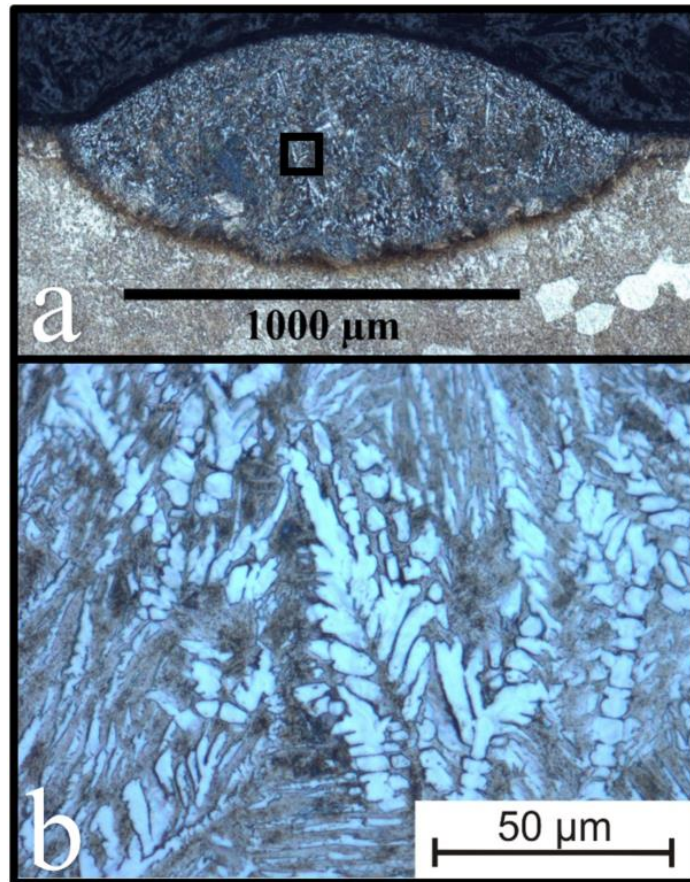
Figure 4-7 Microstructures of clad produced with no auxiliary shielding gas. **a:** Whole clad; **b:** Higher magnification image of the square shown in **a**. The parameters used were: Laser power = 600 W; Laser scan speed = 123 mm/min; Powder feed rate = 4.0 g/min; Powder condition = as-received; Auxiliary shielding gas nozzle type = TIG; Nozzle inner diameter = 15.9 mm
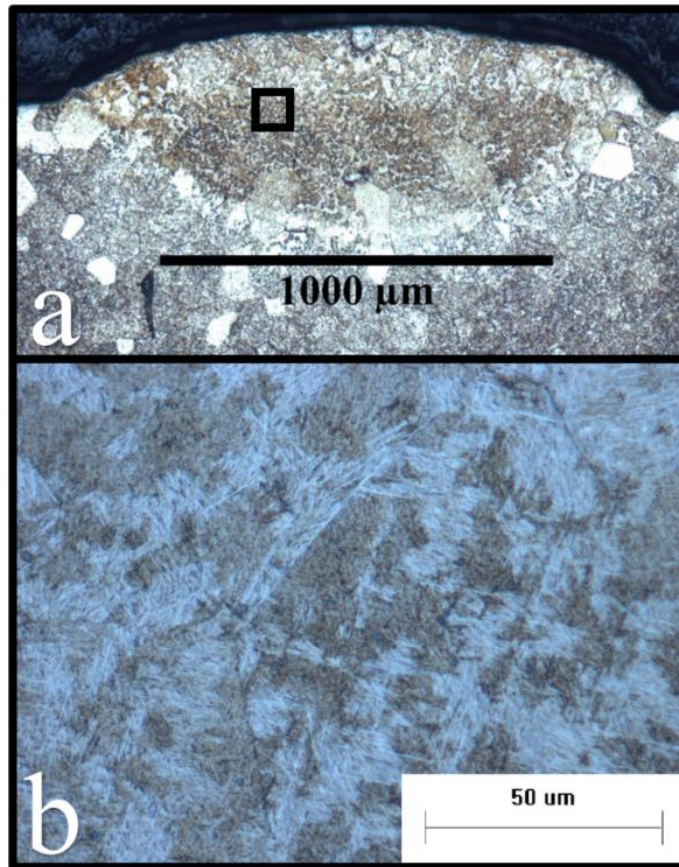
Figure 4-8 Microstructures of clad produced with 14.1L/min of auxiliary shielding gas. **a:** Whole clad; **b:** Higher magnification image of the square shown in **a**. The parameters used were: Laser power = 600 W; Laser scan speed = 123 mm/min; Powder feed rate = 4.0 g/min; Powder condition = as-received; Auxiliary shielding gas nozzle type = TIG; Nozzle inner diameter = 15.9 mm

The present evaluation suggests that it is possible to deposit zirconium with acceptable level of impurities without the need for sealed chamber purged with argon shielding gas. The nozzle design incorporating a modified TIG torch was then used for subsequent experiments. With the objective of creating a small wall, further experiments were conducted to stack a number of clads on top of one another. When no shielding was used, the wall was significantly smaller and more prone to breaking. After about 10 layers, the wall would detach from the

substrate. When adequate shielding was used, the walls would remain firmly attached to the substrate. This observation highlights the importance of adequate shielding for laser cladding and LAM of zirconium.

Chapter 5 – Process Window Development for Laser Cladding[§]

 To choose laser processing parameters that are congenial for LAM, clad quality was assessed based on deposition rate, dilution, geometrical circularity and presence of defects. In this chapter (Harooni et al., 2015; Harooni et al., 2016), the effect of laser power, laser scan speed, laser spot size and powder feed rate on the resulting clad quality was investigated. To allow the results from this chapter to be used on other systems, process maps using combined laser processing parameters were also created. The following processing parameters were controlled in this chapter:

- Powder condition = As-received
- Auxiliary shielding gas flow rate = 14.1 L/min
- Auxiliary shielding gas nozzle type = TIG
- Auxiliary shielding gas nozzle discharge diameter = 15.9 mm
- Argon gas purity ≥ 99.995%
- Angle of nozzle to substrate = 40 ± 5°
- Distance from the powder delivery nozzle to the deposit = 11 mm to 12 mm
- Distance from tip of shielding gas nozzle to tip of powder delivery nozzle = 16 mm
- Number of clad layers = 1

 In order to evaluate the effect of processing parameters with varying laser spot size, laser power and laser scan speed, Steen et al. (2010) graphically compared interaction time (eq. 4-1) and power density (eq. 4-2). Fig. 5-1 compares the power densities and interaction times used in this study to the one reported by Baloyi et al. (2014) and Yue et al. (2012) for cladding zirconium powder, which covered similar values. For this study, clads were deposited using laser spot diameter of 0.9 mm, 1.4 mm and 2.4 mm.

[§] Parts of this section were published in a non-peer reviewed conference paper entitled "Comparison of Nozzle Gas Shielding Techniques for Laser Cladding of Zirconium" at International Congress on Applications of Lasers & Electro-Optics (ICALEO®). Parts of this section were also published in a paper entitled "Processing Window Development for Laser Cladding of Zirconium on Zirconium Alloy" in Journal of Materials Processing Technology
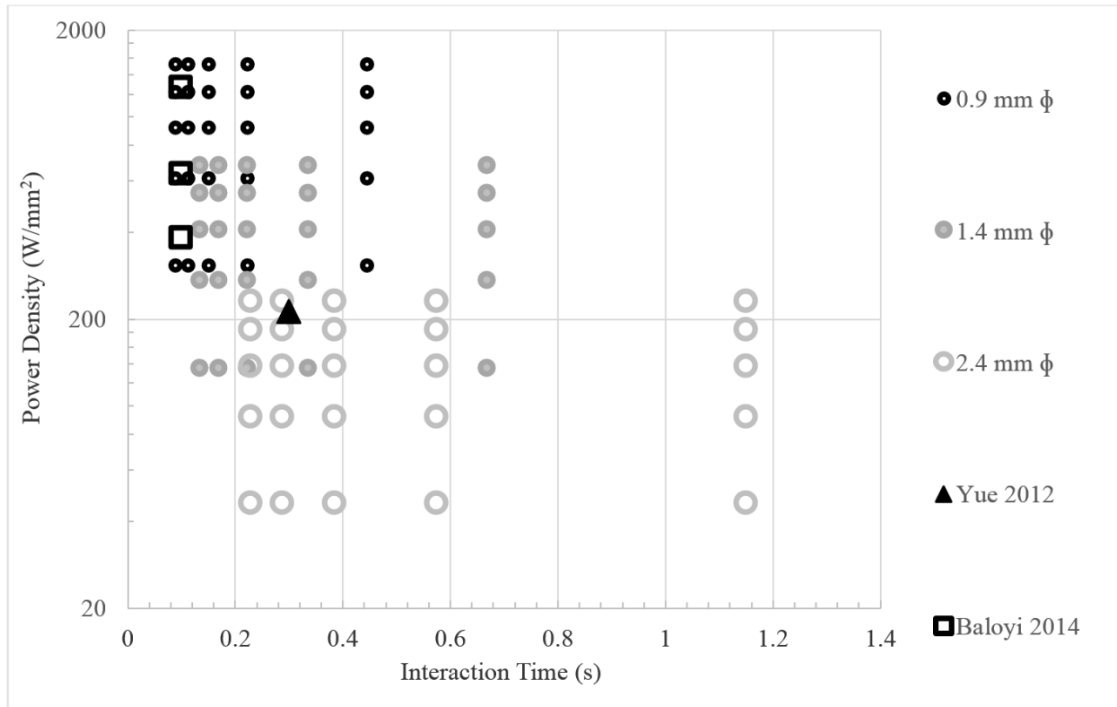
Figure 5-1 Power densities and interaction time

5.1 Effect of Power Density on Defects

Fig. 5-2 compares the power density against interaction time when a powder feed rate of 4 g/min was used. Trends are observed in terms of adherence of the clad, clad symmetry and areas of cavity formation. Based on these criteria, Fig. 5-2 is divided into four main regions. Although both regions A and B consisted of clads that showed uniform and symmetrical geometry with adequate adhesion to the substrate, region A was mainly dominated by clads in which cavities occupied more than 0.5% of the volume fraction of the Fusion Zone (FZ). Although ASTM standards were not used to evaluate the adhesion of the clads, "adequate adhesion" in this work refers to clads that could not be dislodged from the substrate by hand. Region C consisted of clads that had adequate adhesion but showed non-symmetrical or non-uniform geometries. Region D consisted of process parameters that resulted in no observable clads, or those which had inadequate adhesion.

41
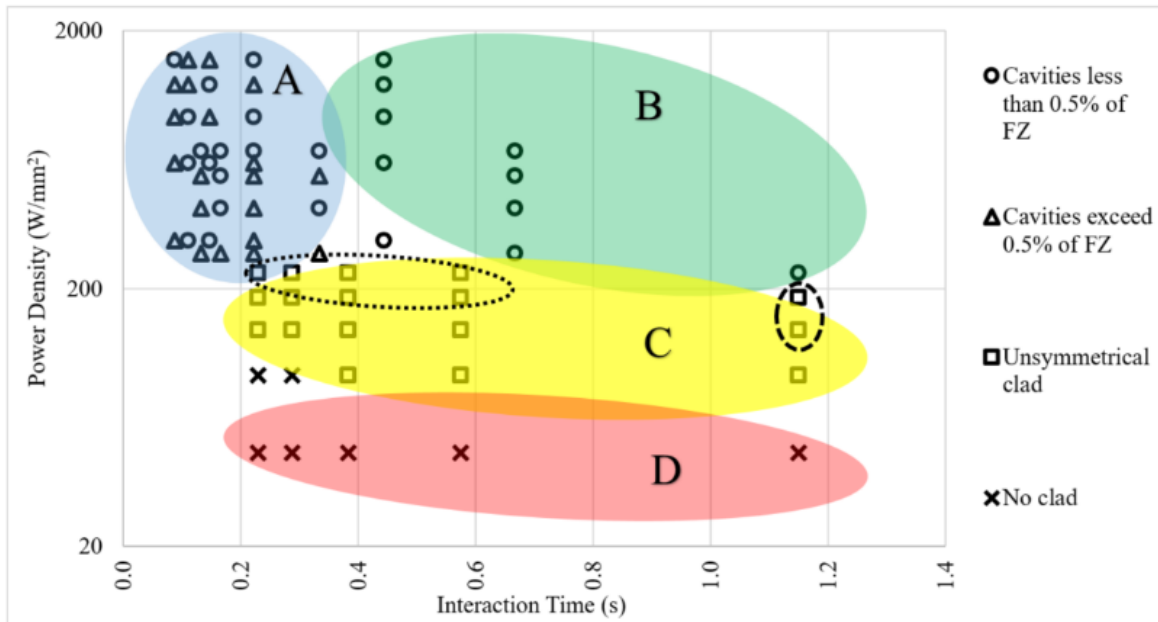
Figure 5-2 Power density versus interaction time. Powder feed rate was 4 g/min

Clads in Regions A and B were formed when sufficiently high power densities were provided for a particular powder feed rate, although in Region A the most common form of defect were cavities. Fig. 5-2 also distinguishes between clads in which cavities occupy more than 0.5% of the volume fraction of the FZ from those which contain less than this value. It also shows that cavities tend to form in Region A where the interaction time is lower than Region B. It is vital to avoid cavity formation, since Carroll et al. (2015) demonstrated that these may contribute to poor ductility in additive manufactured components. The critical value of 0.5% has been selected for Fig. 5-2 since it represents a value which is significantly lower than 1% porosity typically achieved in sintered powder metal as reported by Klar and Samal (2007) or thermally sprayed components as reported by Li et al. (1998).

Two distinct forms of cavities were observed, which will be generally classified here as either spherical (equiaxed) in shape, versus elongated and crescent-shaped as shown in Fig. 5-3. Identifying the mechanism responsible for the different types of cavities is beyond the scope of the present work; nevertheless numerous studies have examined cavity formation in laser

42

welding. In one such study, Meng et al. (2013) attributed the origin of cavities to a complex interaction between the part geometry, molten pool shape, laser induced plasma, and entrapped gases. Matsunawa et al. (1994) showed that pores may form readily when solidification rates are extremely high and the flow of the liquid metal around the laser spot causes turbulence or keyhole collapse. This likely explains why cavities form more readily in Region A where the solidification rates are faster. Courtois et al. (2013) observed the formation of both crescent shaped and equaixed porosity during keyhole collapse experiments. A simulation by Zhou and Tsai (2007) predicted the formation of crescent shaped porosity during keyhole collapse. Nikulina and Malgin (2008) linked the porosity to trace impurities like chlorine, fluorine, magnesium, calcium, potassium and sodium; however it is argued that based on the chemistry measured in Table 4-1, it is not likely that the pores observed are related to impurity gas bubbles. Spherical cavities had an average critical diameter of 35μm with a standard deviation of 20 μm. The critical diameter can be defined as:

$$Critical\ Diameter = 2 * \sqrt{\frac{A_{Porosity}}{\pi}} \qquad \text{(eq. 5-1)}$$

where $A_{Porosity}$ is the area of the area of a porosity.
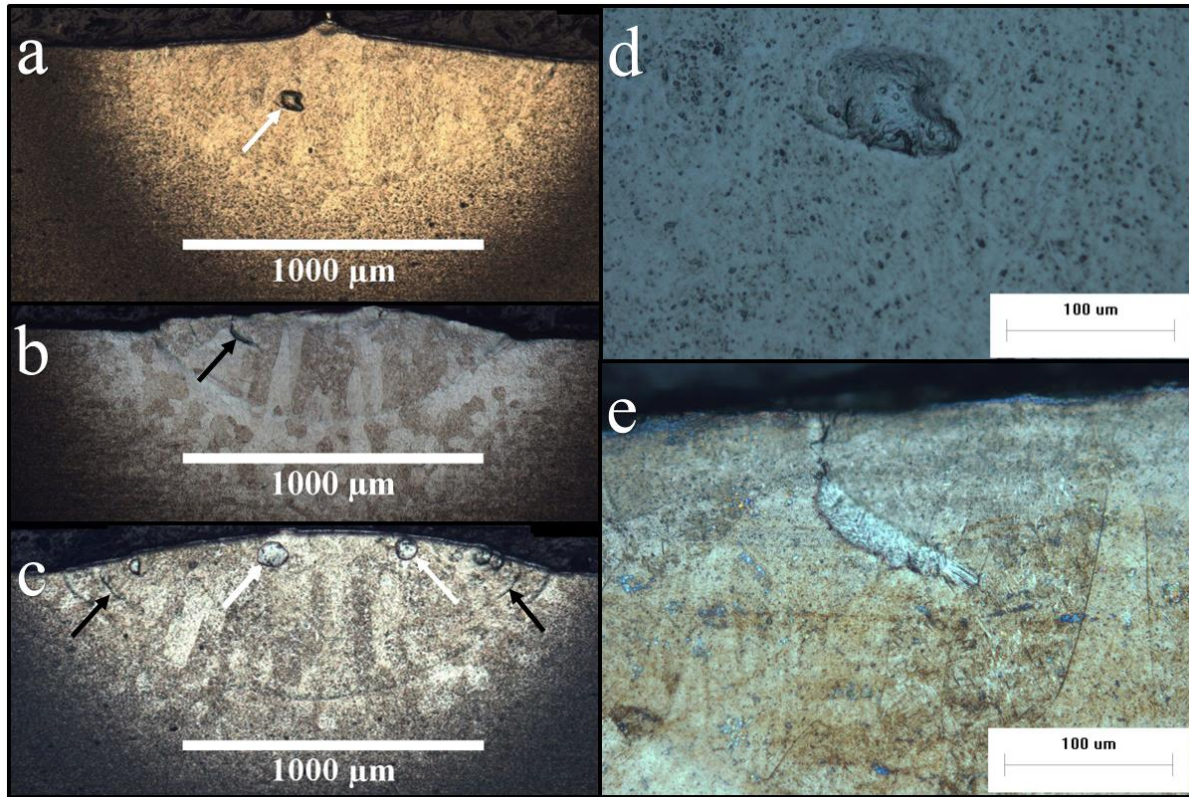
Figure 5-3 Types of cavities observed. White and black arrows point to spherical and elongated cavities respectively. **a:** spherical cavity; **b:** elongated cavity; **c:** spherical and elongated cavities; **d:** higher magnification image of cavity in **a**; **e:** higher magnification image of cavity in **b**

In order to compare the cladding parameters and their influence on cavities, it is useful to calculate the amount of energy used to deposit a gram of zirconium:

$$\bar{E} = \frac{P}{v * A_{above} * \rho} \qquad \text{(eq. 5-2)}$$

where A_{above} is the area of the FZ above the substrate's surface and ρ is the density of zirconium.

It can be noted from Fig. 5-4 that the percentage of the FZ occupied by cavities for clads made using the processing parameters defined by Regions A and B (see Fig. 5-2) diminishes with an increase in the energy used to deposit a gram of zirconium. Although the data presented in Fig. 5-4 does not distinguish between spherical shaped and crescent-shaped cavities, increasing the energy used to deposit a gram of zirconium reduced the percentage of both cavity types.
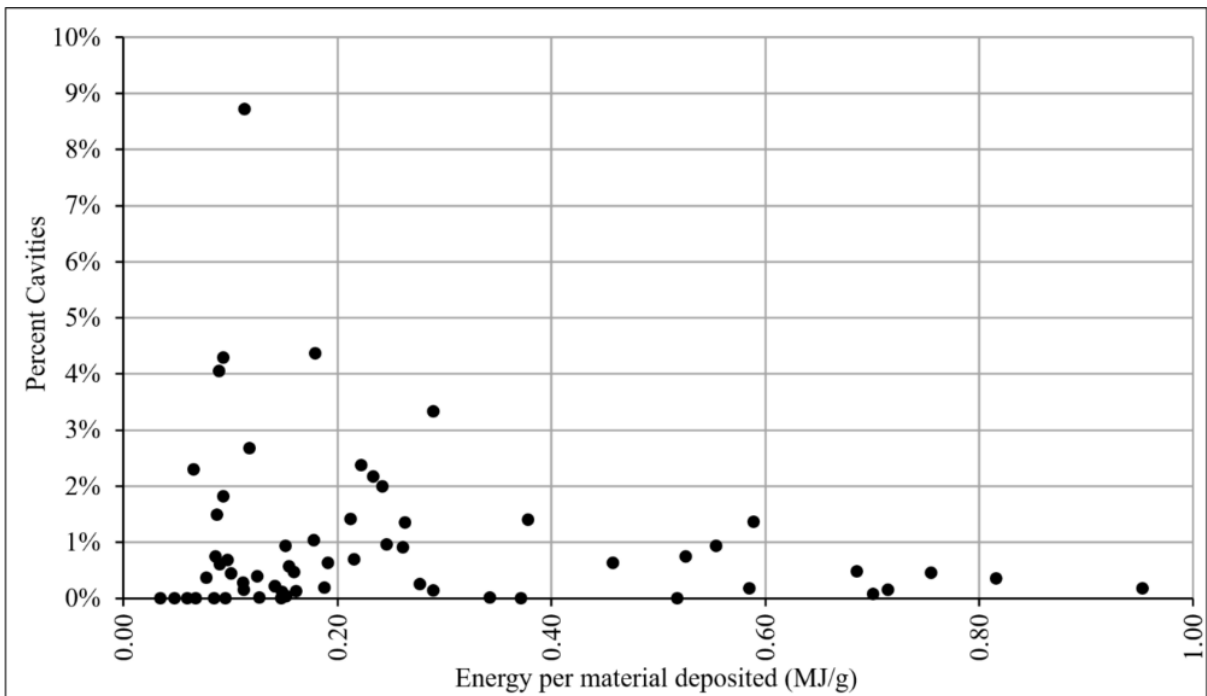
Figure 5-4 Percent cavity and energy used to deposit a gram of zirconium for clads in regions A and B

Although Region C in Fig. 5-2 had a power density that was sufficient to melt some of the powder and the substrate, it was still not high enough to support the powder feed rate used. This led to adequately adherent clads with unsymmetrical geometry as shown in Fig. 5-5. Within Region C, clads with a number of different features were observed. The high power density and high interaction time conditions are highlighted in Fig. 5-2 using a dashed ellipse. This sub-region showed relatively high deposition rates and low dilution rates. Unsymmetrical

clads with high power density but medium to low interaction time resulted in clads with high porosity. This region has also been highlighted in Fig. 5-2 using a dotted ellipse. The rest of the non-highlighted unsymmetrical clads showed very small dilution rates. Fig. 5-5 shows examples of clads from each one of the three unsymmetrical clad sub-regions. Deposition rate, and dilution can be defined as:

$$Deposition\ Rate = v * A_{above} * \rho \qquad \text{(eq. 5-3)}$$

and,

$$Dilution = \frac{A_{below}}{A_{above} + A_{below}} \qquad \text{(eq. 5-4)}$$

where A_{below} is the area of the FZ below the substrate surface. It is important to note that deposition rate is only a fraction of the powder feed rate.
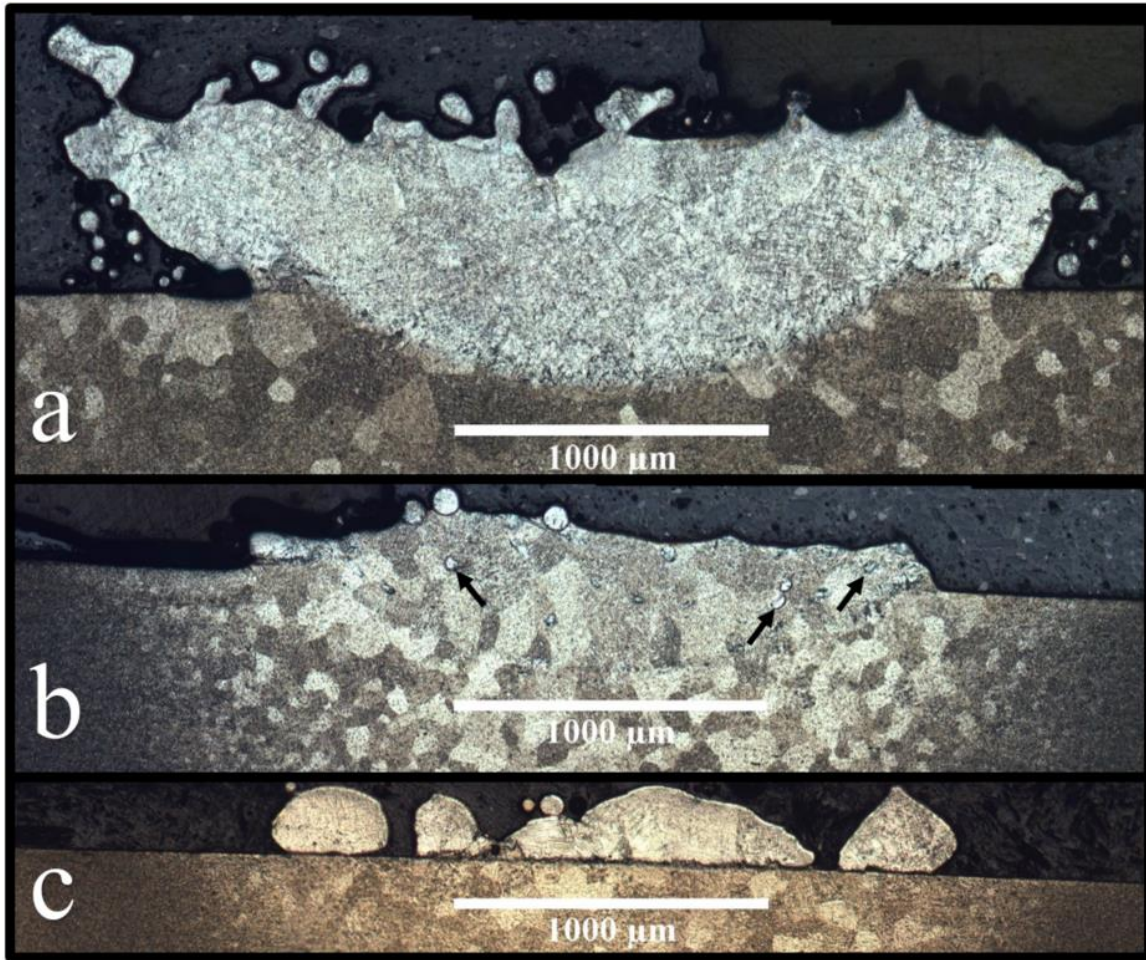
Figure 5-5 Representative unsymmetrical clads from "Region C" of Fig. 5-2 **a:** high power density and high interaction time; **b:** high power density with medium to low interaction time. Arrows indicate cavities; **c:** low power density

In Fig. 5-5c, there is clearly no evidence of substrate melting, indicating only powder melting occurred. This reveals insufficient power density was available to overcome the high cooling rate imparted by the substrate conductivity and its mounting fixture. When the power density was increased while low to medium interaction times were used, the surface of the substrate experienced some melting as indicated by Fig. 5-5b. Since the cooling and solidification rate experienced by these clads was still very high, a number of cavities can be observed. It should be noted that the clads belonging to this sub-region within Region C lie

47

adjacent to Region A which is prone to high porosity. This sub-region can be regarded as a transition region between Region A and Region C. The high power density and high interaction time conditions within Region C allow more of the powder and the substrate to melt. The longer interaction time allowed more powder to mix with the existing melt pool, resulting in a large unsymmetrical clad shown in Fig. 5-5a. When processing parameter corresponding to Region D of Fig. 5-2 were used, the cooling rates were too high to allow sufficient melting of the substrate, leading to poor clad adhesion.

As shown in Fig. 5-6, when the powder feed rate was increased from 4 g/min to 8.8 g/min the trends observed in Fig. 5-2 shifted towards obtaining more suitable cladding parameters with interaction times > 0.3 s. It can be observed that clads in which cavities occupy less than 0.5% of the FZ are still produced with higher interaction times and power densities, with unsymmetrical clads produced at power densities < 500W/m^2, and clads with excessive cavities occurring with at interaction times << 0.3s. The trends are expected to change when other process parameters like powder size, preheating and other factors are varied.
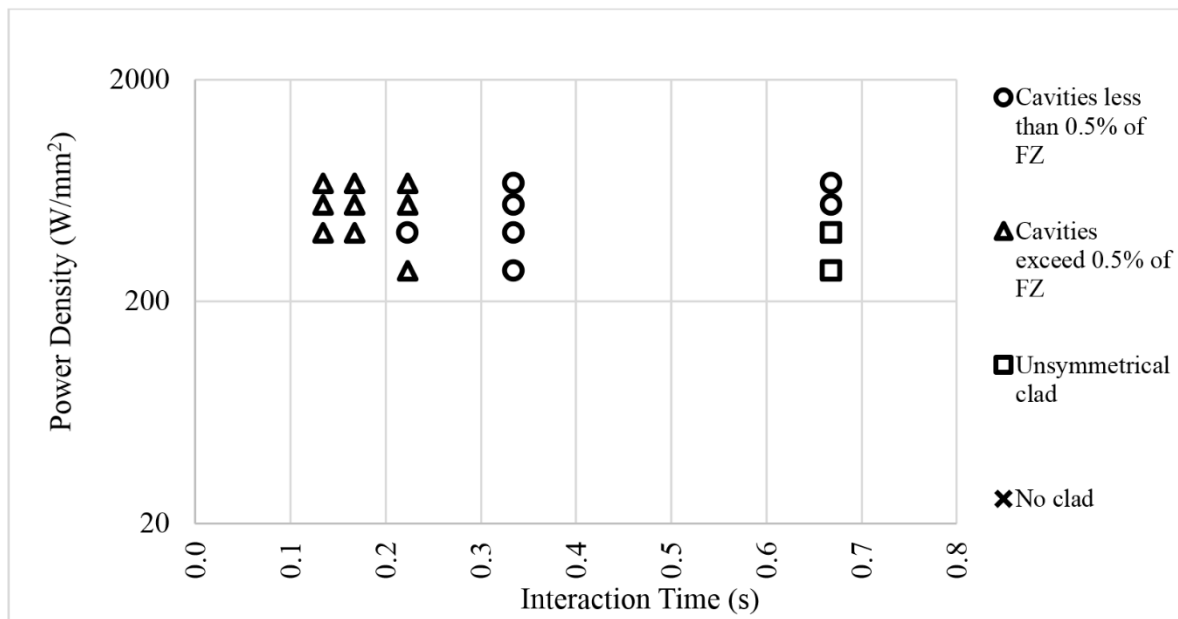
Figure 5-6 Power density versus interaction time. Powder feed rate was 8.8 g/min

Apart from the defects mentioned above, some well adherent clads with symmetrical geometries showed undercut, and mushrooming defects as shown in Fig. 5-7. Based on the comparison of the geometry, adhesion and cavity formation with various parameters studied here, clads were selected for further additive manufacturing which were symmetrical and well adhered to the substrate. Furthermore, these clads had no cavities in them and showed no mushrooming or undercutting defect.
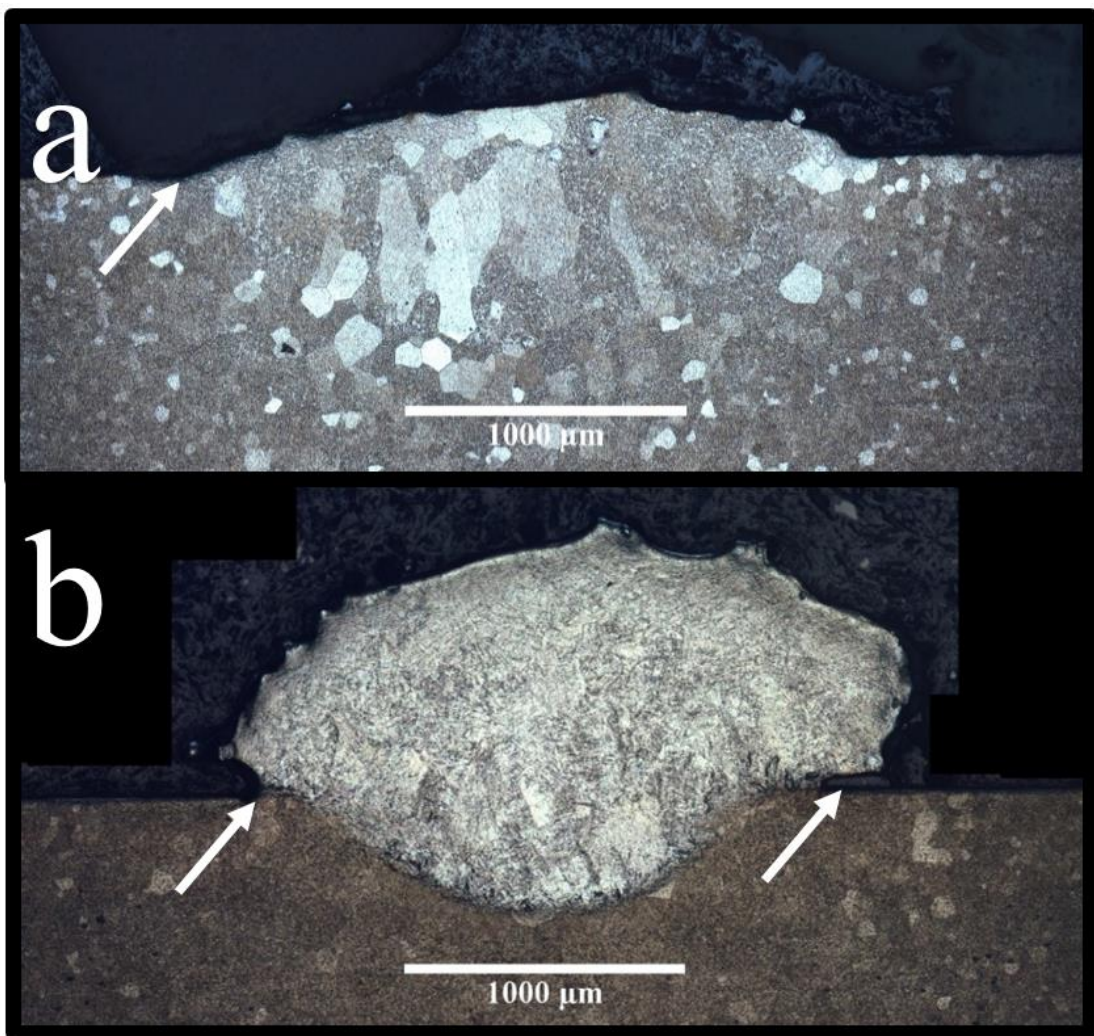
Figure 5-7 Arrows indicate points of interest. **a:** undercut defect; **b:** mushrooming defect

5.2 Microstructural Analysis

The effect of laser scan speed on the clad microstructure is shown in Fig. 5-8. The FZ and the Heat Affected Zone (HAZ) decrease with increasing laser scan speed. The micrographs of the clad produced at the laser scan speed of 245 mm/min shows the transition of microstructure from base metal to FZ. The lighter area on the very right of this micrograph shows the base metal. Moving towards the FZ, this area transitions into a darker region that comprises of grains that are smaller than the base metal. The heat from cladding allowed the heavily cold worked substrate to recrystallize and form grains that were smaller than the base metal. Progressive grain growth can be observed between this region and the FZ. Accelerated grain coarsening in the substrate HAZ is expected considering the highly refined base metal grain size has a large driving force for grain growth upon heating when the initial grains are highly refined and work hardened following rolling of the thin sheet, as in the heavily cold worked zirconium alloy substrate.

Fig. 5-8 also shows epitaxial grain growth within the FZ as suggested by the prior-beta grain structures revealed by optical microscopy. In the case of the 123 mm/min travel speed, the edge of the clad exhibits a wetting angle around 90º, however good adhesion with the substrate can be observed. Lustman and Kerze (1955) stated that upon cooling through the transus temperature, zirconium and its alloys transform from a high temperature BCC beta phase to a low temperature HCP alpha phase. Although the FZ structures in Fig. 5-8 reveal coarse prior-beta grains, the alpha phase grains which comprise the microstructure are significantly finer. Fig. 5-9 shows a higher magnification micrograph of the area indicated by the arrow shown in Fig. 5-8. Campbell (2008) mentioned that zirconium has properties very similar to titanium. Based on the micrographs of titanium alloys presented by Campbell (2008), it can also be noted that the final microstructure of the FZ comprised of very fine alpha or martensitic needles.
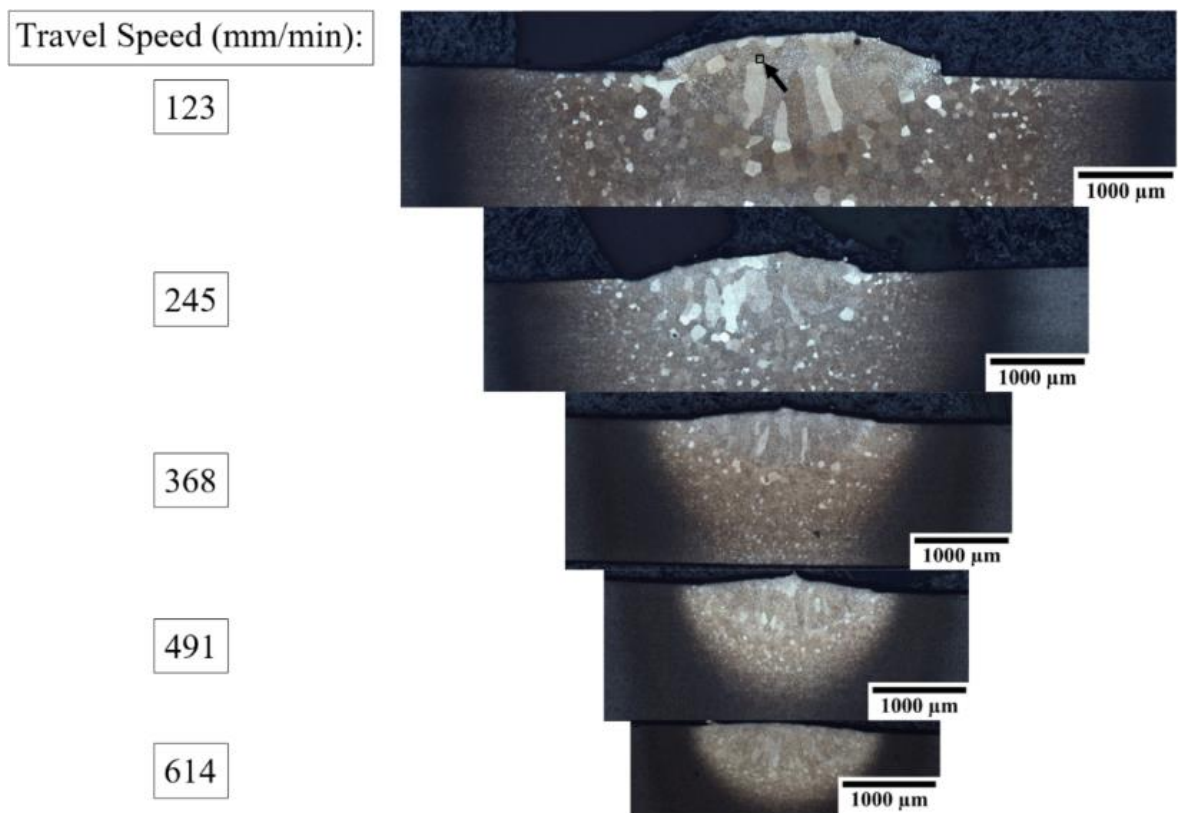
Figure 5-8 Effect of laser scan speed. A higher resolution image of the area indicated by the arrow has been shown in the next figure. The parameters used were: Laser power = 1000W; Laser spot diameter = 1.4 mm; Powder feed rate = 4.0 g/min
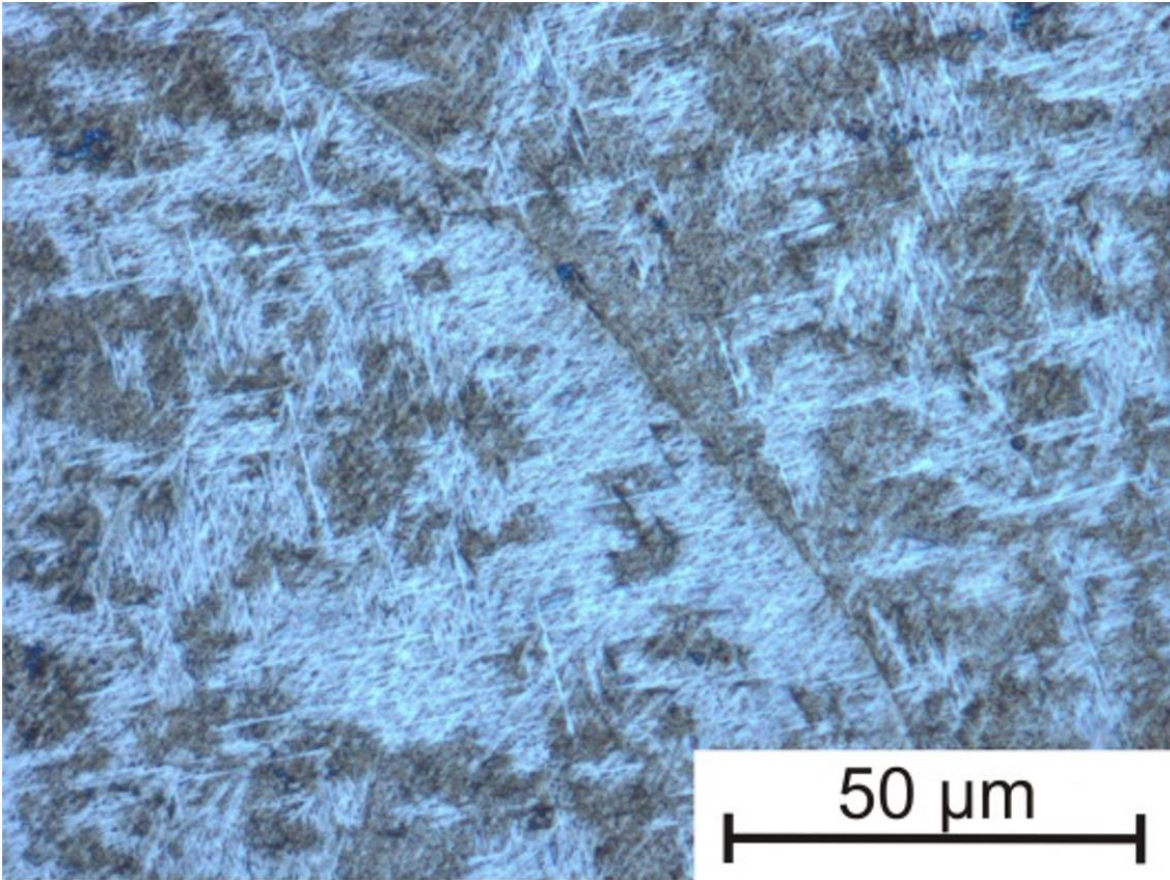
Figure 5-9 Optical micrograph showing the FZ microstructure indicated by the arrow in Figure 5-8.

In a laser additive manufactured Ti-6Al-4V component, Carroll et al. (2015) observed higher ductility in the direction parallel to the longer axis of the prior beta gains than their shorter axis. They hypothesized that this difference was due to grain boundary alpha decorating the prior beta grain boundaries. Carroll et al. (2015) suggested that the properties of additive manufactured components are not just dependant on processing parameters but also on their thermal histories, which can be quite localized and geometry dependant. The use of an open loop system with constant processing parameters will make it impossible to keep consistent thermal history throughout a complex geometry.

Campbell (2008) mentioned that the weldability of titanium alloys decrease with increase in beta stabilizer concentration. A similar relationship is expected for zirconium alloys. Sattari et al. (2013) reported that Nb and Mo act as a beta stabilizer in a Zr-3.5%Sn-0.8%Nb-0.8%Mo alloy. When they quenched this alloy from several processing temperatures, they observed the formation of retained beta phase, athermal omega phase, α'-HCP martensite and α''-orthorhombic martensite. Beta stabilized zirconium alloys are expected to be less suitable for laser additive manufacturing because thermal histories can induce a number of different phases in them. This in turn will result in a variation in properties throughout their geometry.

5.3 Deposition Rate, Dilution and Bead Geometry

The effect of laser power and laser scan speed was analyzed with the objective of identifying clads with high deposition rate, low dilution and good geometry. To quantitatively compare the geometry of the clads, a combined parameter called circularity was used. Ferreira and Rasb (2012) used this parameter in an image analysis software entitled "ImageJ". It was found that as the value of circularity approached 1, the clad became more symmetrical and consistent. Ferreira and Rasb (2012) defined circularity as:

$$Circularity = \frac{4\pi * (A_{above} + A_{below})}{Peri^2} \qquad \text{(eq. 5-5)}$$

where $Peri$ is the perimeter of the FZ.

Fig. 5-10 shows the effect of laser power and laser scan speed on deposition rate, dilution and circularity. For a given laser power, lowering the laser scan speed would result in higher deposition rate, lower dilution and higher circularity values. Increasing laser power increases deposition rate and circularity, however there is a trade-off in that decreasing laser

power results in lower dilution with the substrate. Ideally, for a well-controlled additive manufacturing process, some compromise would need to be reached between geometry and dilution, since the cladding will no longer adhere to the substrate if some minimum dilution is not achieved.
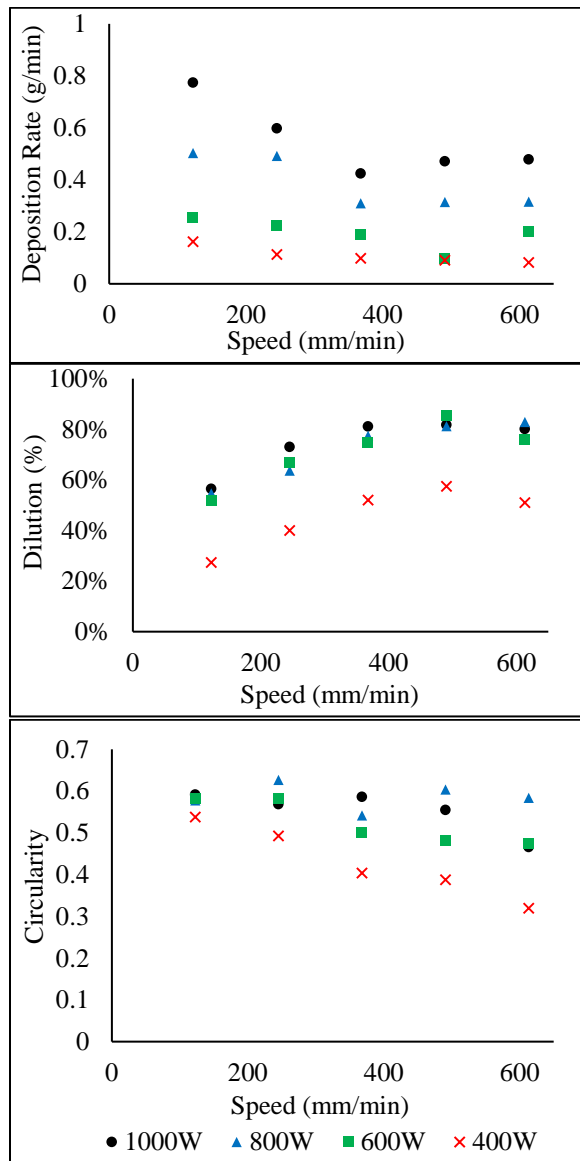
Figure 5-10 Effect of laser power and laser scan speed on deposition rate, dilution and circularity. The parameters used were: Laser spot diameter = 1.4 mm; Powder feed rate = 4.0 g/min

Fig. 5-11 shows the effect of laser spot diameter, powder feed rate and laser scan speed on deposition rate, dilution and circularity. The three laser spot diameters evaluated were: 0.9 mm, 1.4 mm and 2.4 mm. The two powder feed rates tested were: 4.0 g/min and 8.8 g/min. As previously noted, lowering laser scan speeds resulted in a better deposition rate, dilution and circularity. Although increasing the laser spot diameter to 2.4 mm improved deposition rate and dilution, the geometry of the clad was compromised. Reducing the laser spot diameter to 0.9 mm improved clad geometry at the expense of deposition rate and dilution. Maintaining the laser spot diameter at 1.4 mm but increasing the powder feed rate to 8.8 g/min provided a compromise between these outputs, where increased deposition rate and circularity are achieved with lower dilution.
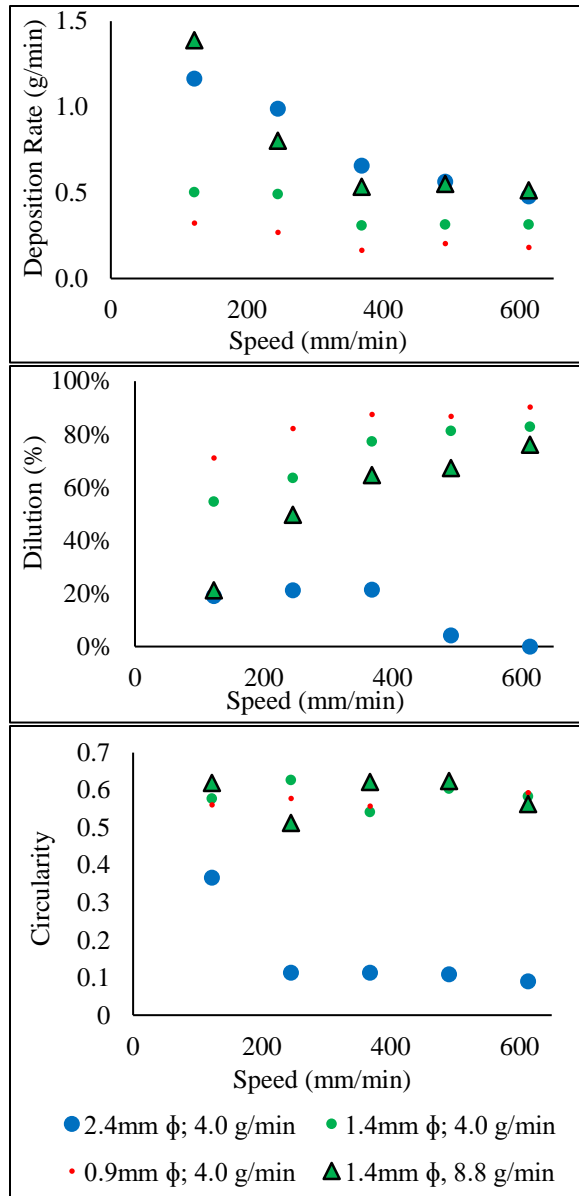
Figure 5-11 Effect of laser spot diameter, powder feed rate and laser scan speed on deposition rate, dilution and circularity. Laser power of 800W was used.

5.4 Identifying Parameters for Zirconium Powder Deposition

56

To determine feasible parameters which may be applied during the deposition, clad quality was assessed for clads produced with a laser spot diameter of 1.4 mm and powder feed rate of 8.8 g/min. The selection process was further restricted to the group of clads that were produced using laser scan speed of 123 mm/min and 245 mm/min. Among the remaining clads, the ones produced with a laser scan speed of 123 mm/min either showed mushrooming defect or had unsymmetrical geometries. The clads produced at 245 mm/min were screened for cavities, undercuts and mushrooming defects. Based on the screening process, the two clads that exhibit potential for laser additive manufacturing are shown in Fig. 5-12. The smaller of the two clads was produced at 400W and yielded dilution of 24%, circularity of 0.58 and a deposition rate of 0.28 g/min. The larger clad was produced at 800W and resulted in dilution of 50%, circularity of 0.51 and deposition rate of 0.80 g/min.
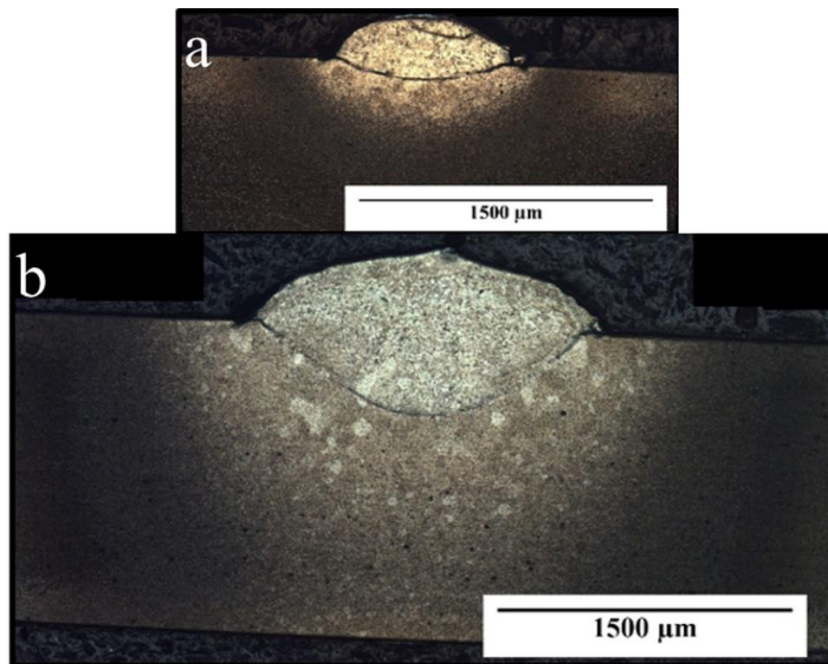
Figure 5-12 Clads showing the greatest potential for laser additive manufacturing. Common parameters used for the clads: Laser spot diameter = 1.4 mm; Laser scan speed = 245 mm/min; Powder feed rate = 8.8 g/min; **a:** Laser power = 400W; **b:** Laser power = 800W

Chapter 6 – Comparing Mechanical Properties and Microstructure of Zirconium Deposit Fabricated Using Laser Additive Manufacturing

The purpose of this chapter was to determine if LAM of zirconium components was possible while maintaining satisfactory microstructures and mechanical properties compared to commercial zirconium alloys. The purpose of this chapter was also to compare the properties of deposits made using recycled and as-received powder and investigate the fracture behaviour during tensile testing. The laser processing parameters chosen in the previous chapter were used to create multiple layered clad deposits using recycled and as-received powder. The test case examined was a narrow wall produced by repeatedly depositing clad lines on top of one another. The results from this chapter can allow nuclear, biomedical and chemical processing industries to consider using LAM zirconium parts instead of conventionally manufactured parts. The following processing parameters were controlled during the multilayer deposited wall structures:

- Laser spot diameter = 1.4 mm
- Laser scan speed = 245 mm/min
- Powder feed rate = 8.9 g/min
- Recycled powder sieve size range = 44 µm to 105 µm
- Auxiliary shielding gas flow rate = 33.0 L/min
- Auxiliary shielding gas nozzle type = TIG
- Auxiliary shielding gas nozzle discharge diameter = 15.9 mm
- Argon gas purity ≥ 99.999%
- Angle of nozzle to substrate = 45 ± 3°
- Distance from the powder delivery nozzle to the deposit = 10 to 11 mm
- Distance from tip of shielding gas nozzle to tip of powder delivery nozzle = 3 mm
- Dwell time between two consecutive passes = 5 s

6.1 Deposition Properties

While making the laser depositions, the cladding was only applied in one direction. After the creation of each clad layer, the laser head and the powder delivery nozzle stayed at the end of the clad for 5 seconds before travelling back to the starting point of the deposit. This dwell time was introduced to provide sufficient shielding to the end of the deposit. After each clad layer, the CNC machine was also programmed to raise the height of the laser head and the powder delivery nozzle by the amount specified in Table 6-1. This was done to ensure that the laser spot diameter and the distance from the powder delivery nozzle to the deposition remained approximately constant as the deposition was being built. To determine the appropriate height increment between two consecutive clad layers, smaller 10 clad layer deposits were made with varying height increments. The height increment setting that was most successful at maintaining the distance between laser head and the top of the deposition was chosen for making the laser depositions. It was found that the growth of the deposition was very dependant upon parameters like laser power and distance of the powder delivery nozzle to the deposition. This made it necessary to determine the height increment after any adjustment to the nozzle setup or prior to using a new set of laser processing parameters. For instance, Fig. 6-1c shows a deposition that was successfully made when the distance from the powder delivery nozzle to the deposition was 10 mm. When this distance was increased from 10 mm to 12 mm while all other processing parameters were kept constant, the resultant deposition was misshaped and heavily discoloured. It is believed that increasing this distance reduced the amount of powder that was reaching the melt pool. This stunted the growth of the deposition and caused misalignment between the powder delivery nozzle and the deposition. As the misalignment increased, less and less amount of powder and shielding could reach the deposition.

Compared to the height of a single layer clad on a flat substrate, the height of clads in multilayer deposits were 45% to 97% taller. This implies that heat dissipation was poorer for multilayer clads, since a greater amount of retained heat in the substrate will promote higher deposition efficiencies and higher build rates. The geometry of the deposition wall and the preheating of the deposition by previous cladding passes are believed to be responsible for

59

reducing the heat dissipation. Table 6-1 lists the parameters that were varied to create the deposits shown in Fig. 6-1.

Table 6-1 Parameters used to create the deposits shown in Fig. 6-1

Powder condition	Recycled	Recycled	As-received
Laser power (W)	800	400	800
Number of clad layers	50	60	56
Height adjustment of nozzle and laser in build direction after each clad (mm)	0.617	0.502	0.702

A common feature of all the depositions shown in Fig. 6-1 is that they all fit in an outline of a right trapezoid in the build-cladding direction plane. The acute angle of the trapezoid measured 64°, 55° and 66° for 800 W recycled, 400 W recycled and 800 W as-received powder deposits respectively. Larger angles are associated with a greater ease with which a stable melt pools was established during deposition. The lower heat input generated by the 400 W laser power was less effective at creating the melt pool and preheating the previously deposited clad layers. This resulted in the discontinuous deposition shown in Fig. 6-1b. Fig. 6-1b also shows a lack of fusion between the deposition and the substrate. Unlike the other depositions shown in Fig. 6-1, the 400 W deposition dissociated from the substrate when pushed with a finger. In Chapter 5, it was shown that lower laser power resulted in a lower dilution. One of the reasons for the poor adhesion of the 400 W deposition can be attributed to the lower dilution rate. It is believed that if the powder and/or the substrate could be preheated, a more adherent and continuous deposition can be created with the same laser processing parameters. Since the 400 W recycled powder deposition reported in Fig. 6-1 was clearly unsuitable for additive manufacturing, it was not analyzed any further for this work.

By comparing the 800 W recycled and as-received powder deposits in Fig. 6-1, it can be observed that the incline created by the right trapezoid is rougher for the recycled powder deposit. This suggest that the melt pool was more unstable when recycled powder was used.

The melt pool later became stable after a few millimeters of travel, and resulted in continuous deposition.

Table 6-2 shows the results of an inert gas fusion analysis that was performed on similar regions on the 800 W deposits. It can be observed that the oxygen and nitrogen content were very similar suggesting that the bulk material experienced an absorption limit. AWS (2012) states that zirconium turns from silver to straw/gold, to intermediate colours, until finally a powdery white/yellow is produced when it is heated above 427°C in an atmosphere with unacceptable level of atmospheric contamination. It also states that acceptable zirconium welds can only be silver or dark straw in colour. The 800 W recycled and as-received powder deposits in Fig. 6-1 show purple discolouration towards the top left corner. The top left region was the most susceptible to discolouration because it stayed at elevated temperatures for the longest time. This region experienced heat not only from previous cladding layers but also from continuation of laser irradiation to make the rest of the clad layer. The presence of purple discolouration in the top left corner indicates that more shielding is required in some regions of the deposit than others. As shown in Chapter 4, this can be accomplished using a larger gas lens with proportionally increased shielding gas flow rate. Alternatively, a trailing gas shield can also be used. Fig. 6-1 also shows that the surface of 800 W recycled powder deposit experienced more severe discolouration than the 800 W as-recieved powder deposit. This is likely due to the higher energy deposition conditions that were created with recycled powder because of a smaller build direction height increment between clads.

Table 6-2 Chemical composition of recycled and as-received powder deposits. Laser power was 800 W.

Component (ppm)	Recycled	As-received
N	350	330
O	4300	4300
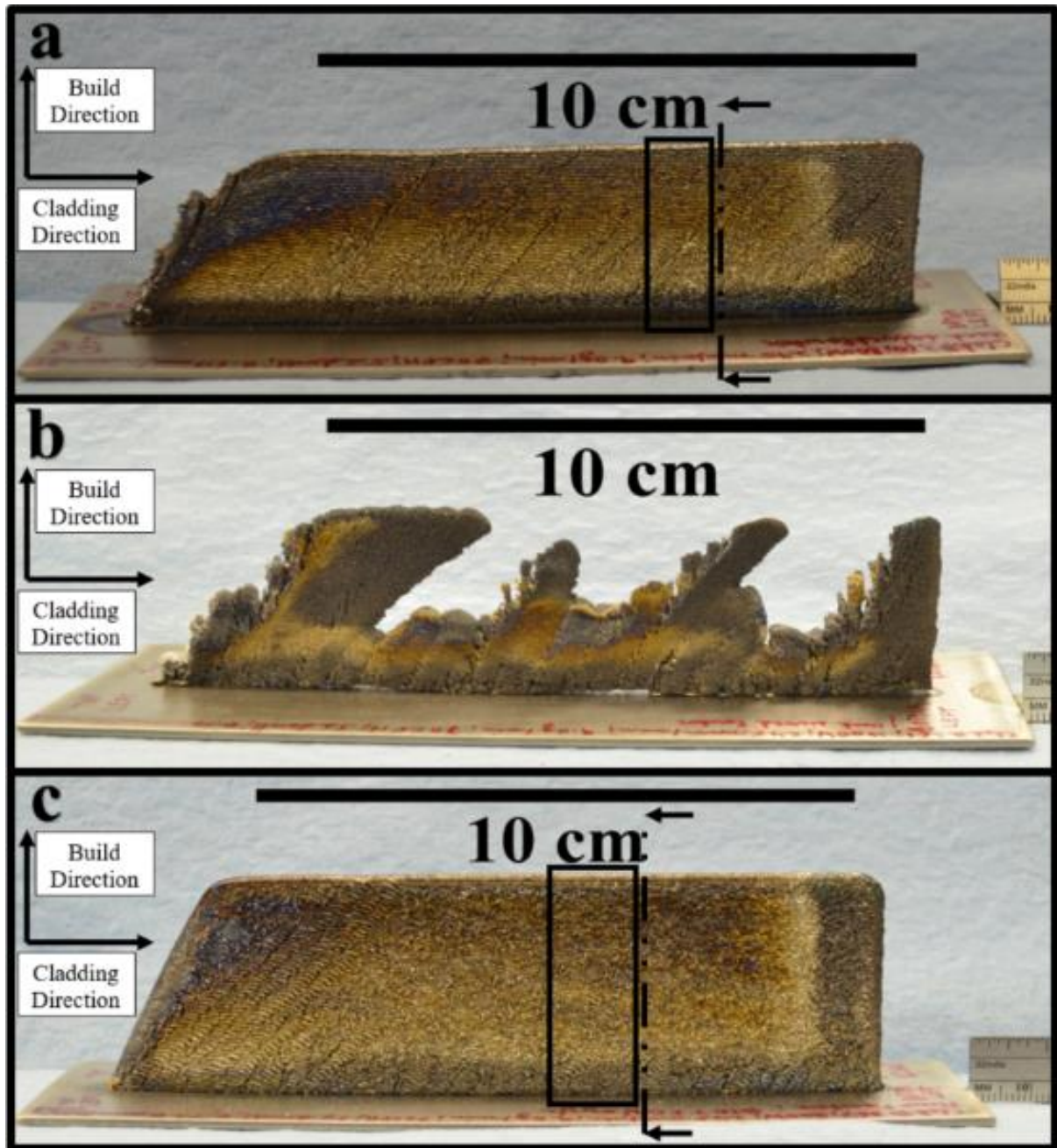
Figure 6-1 Effect of powder condition and laser power on deposition. **a:** powder condition = recycled and laser power = 800 W; **b:** powder condition = recycled and laser power = 400 W; **c:** powder condition = as-received and laser power = 800 W;

Fig. 6-2 shows a cross sections of 800 W recycled and as-received powder deposition along the sectioning lines shown in Fig. 6-1. The figure shows that the successive layers within the deposition adhered well with full metallurgical bonding to each other.
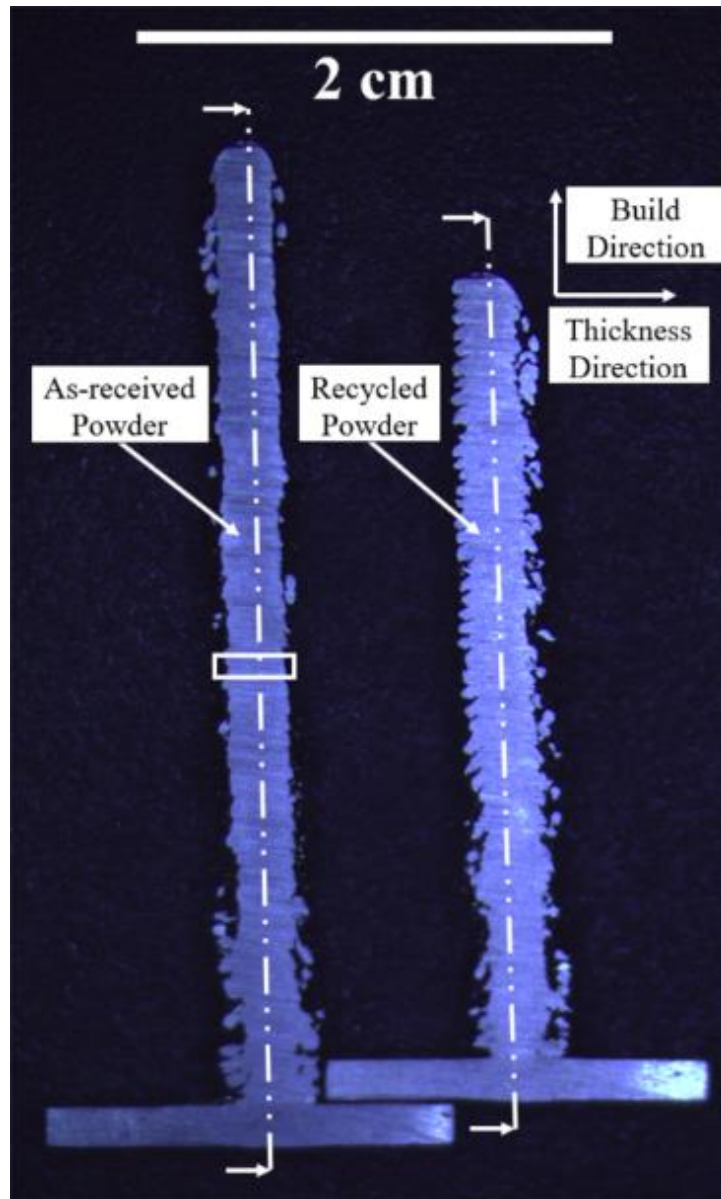
Figure 6-2 Cross-section of as-received and recycled powder deposition along the lines shown in previous figure. Laser power was 800W.

Fig. 6-2 was used to calculate the deposition properties shown in Table 6-3. The catchment efficiency was calculated as:

$$Catchment\ Efficiency = \frac{Deposition\ Rate}{(n*\dot{m})} = \frac{(v*A_{above}*\rho)}{(n*\dot{m})} \qquad \text{(eq. 6-1)}$$

where n is the number of clad layers used in the deposition and $\dot{m}$ is the powder feed rate.

From the work presented in Chapter 5 on single layer clads, processing parameters similar to the ones used for making deposits in Table 6-3 resulted in a catchment efficiency of only 9.2%. The much higher deposition rates of the multilayer clad deposits highlights the differences between their deposition properties versus the single layer clads. The higher deposition rate can be attributed to preheating of the deposition by previous cladding layers. The geometry of the deposition is also believed to be less efficient at dissipating heat compared to a flat substrate.

Fig. 6-2 shows that the sides of the deposition walls were fairly rough. Table 6-3 predicts that if the deposition was detached from the substrate and its surfaces were milled to get rid of all the asperities, only about half of the deposition would be available for use. It is believed that with further refinement of processing parameters, the roughness of the wall could be reduced. Table 6-3 also shows that the total height increment of the laser head and the powder delivery nozzle during the deposition was very close to the total height of the deposit. This suggests that the laser head and powder delivery nozzle remained aligned with the top of the deposit during the deposition process. In general, the deposition properties of the recycled and as-received powder deposits were quite similar.

Table 6-3 Deposition properties of the 800W recycled and as-received powder deposits

Powder condition	Recycled	As-received
Catchment efficiency	35%	34%
Total width of deposition (mm)	4.3	4.5
Percentage of deposition thickness available after machining away asperities	46%	54%
Total height adjustment of the laser and nozzle in build direction: Actual height of deposition	0.95	0.99

6.2 Microstructure and Porosity

Fig. 6-3 shows a higher magnification image of the white rectangle shown in Fig. 6-2. Some grain boundary α can be seen decorating prior β grains. In some instances parallel laths are seen originating from the prior β grains. The figure shows that large and mainly parallel lath structure occupies the edges while a finer and mainly Widmanstätten laths structure occupies the center of the deposit. The microstructure of the 800 W recycled powder deposit from a similar region was very comparable.
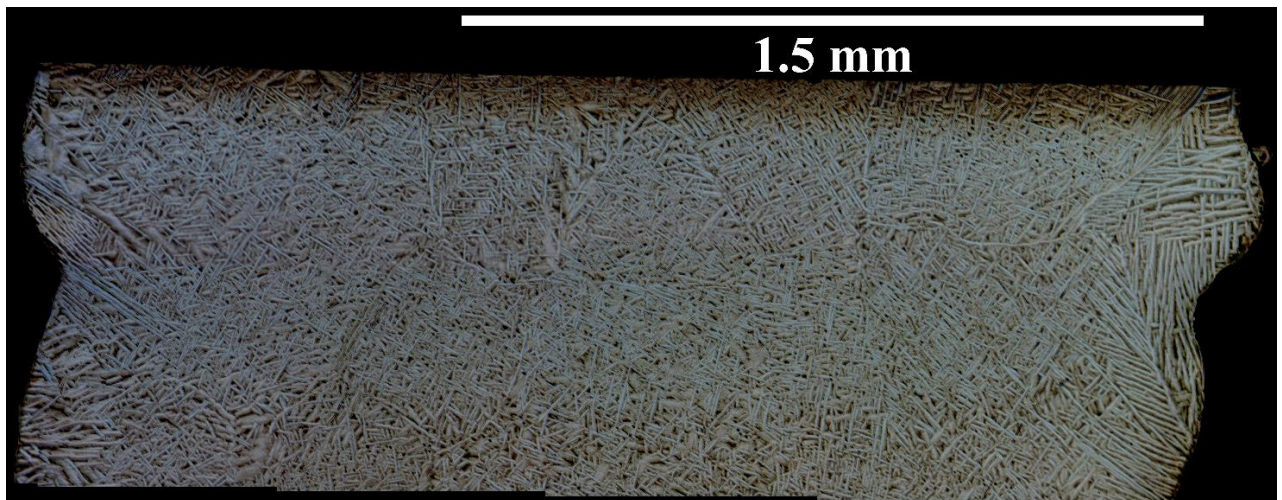
Figure 6-3 Higher magnification image of the area shown in previous figure

Fig. 6-4 shows a cross section from the center of the 800 W recycled powder deposit along the sectioning line shown in Fig. 6-2. The sample was taken from the top region of the black rectangle shown in Fig. 6-1. Fig. 6-4b shows a microstructure very similar to the one observed from the center of the clad in Fig. 6-3. It was also comprised predominantly of fine Widmanstätten laths structure. Some grain boundary α was observed around prior β grains and parallel lath structure was noticed originating from it. Similar observations were also made for the as-received powder deposit.

Fig. 6-4a revealed that faint striations were present in the sample, parallel to the cladding direction. Closer inspection of the striations revealed that darker bands had finer microstructure. The repeating microstructural size change in the build direction suggests that the deposit experienced a range of thermal history. Striations were observed in as-received powder deposit as well. Frazier (2014) also observed striations in LAM components made using materials other than zirconium.

In general, changes in size and arrangement of the laths were observed along thickness direction. Periodic variation in size of the microstructure was also observed in the build direction. Since the deposition experienced a number of thermal histories, it is also possible that a non-equilibrium and equilibrium phases might coexist in the deposit.

The microstructure of single and multi-layers deposits were very similar. They were both made up of fine α Widmanstätten laths surrounded by grain boundary α along prior β grains. As seen by Fig. 5-7a and Fig. 5-8, single layer deposits showed columnar prior β grain structure originating from the fusion line of the clad and more equiaxed prior β structure towards the top most point of the clads. Similarly, equiaxed prior β structure was also observed at the top most portions of the as-received and recycled powder deposits.

Porosity can also be observed in Fig. 6-4. Table 6-4 shows that pores were fairly circular. Fig. 6-5 shows that the porosity size distributions for both as-received and recycled powder

deposit were comparable to the powder size used for the deposition, however the recycled material promotes much larger pore sizes. According to Michael Wright of CNL, the level of porosity observed in recycled powder deposit was comparable to zirconium welds. He also mentioned that recycled powder deposits made using DED LAM technology appear to have lower porosity levels than deposits made using as-received powder by PBF LAM technology (Wright, 2015). Since most pores were comparable to the powder size, this may suggest that the major source of the porosity was unmelted or partially melted powder particles. As shown by Fig. 6-4b, some pores were surrounded by finer microstructure. In fusion welding, finer microstructure exist in areas that are the last to solidify. These areas are more prone to elemental segregation. Abriata et al. (1986) and Gribaudo et al. (1994) reported that both oxygen and nitrogen increase the solidification temperature of molten zirconium. Oxygen and nitrogen from the powder or picked up during deposition process is expected to concentrate around the pores. Lustman and Kerze (1955) reported oxygen and nitrogen as being interstitial impurities that increase hardness and tensile strength at the expense of ductility. This implies that the regions around the porosity are expected to be harder and less ductile than the rest of the deposition.

Table 6-4 also shows that porosity in as-received powder deposit had a smaller average critical diameter, were less common and were less clustered than in recycled powder deposit. Fig. 6-5 demonstrates that the variation in porosity size of as-received powder deposits was smaller. Since Table 6-2 shows little variation in the oxygen and nitrogen content of the bulk recycled and as-received powder deposits, it appears that most of the pores were caused by a small fraction of powder particles that had experienced severe atmospheric contamination. These particle would have higher melting point which will make them more difficult to dissolve. It follows that porosity can be minimized by separating these heavily contaminated particles. It might also be possible to reduce the influence of these particle by a post-process Hot Isostatic Pressing (HIP) treatment. The process could potentially dissolve oxides and minimize porosities.
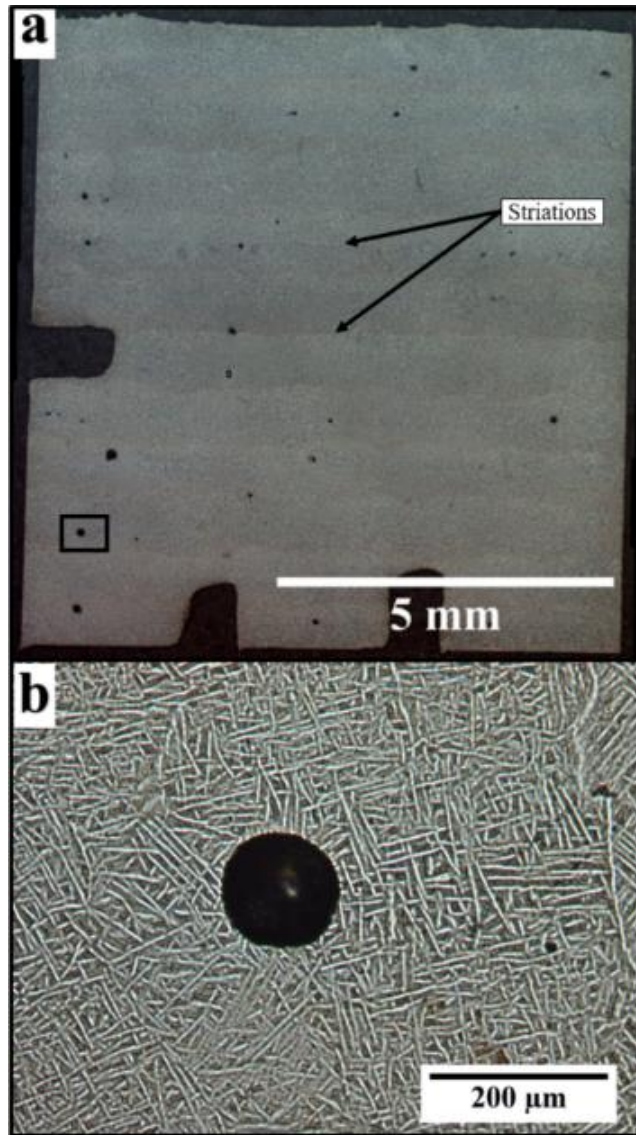
Figure 6-4 Micrograph of the recycled powder deposition taken from the top of rectangular box shown in Fig. 6-1 and along the cross sectional lines shown in Fig. 6-2. **a**: striations; **b**: higher magnification image of the rectangle shown in **a**.

Table 6-4 Properties of porosity found in 800W recycled and as-received powder deposits

Powder condition	Recycled	As-received
Area analyzed (mm^2)	148	145
Pore density (pores/ mm^2)	0.43	0.13
Average spacing between adjacent porosity (µm)	1519	2762
Minimum observed spacing between two adjacent porosity (µm)	4.9	13.1
Area% Porosity	0.099%	0.010%
Average critical diameter (µm)	41	28
Average circularity	0.40	0.44
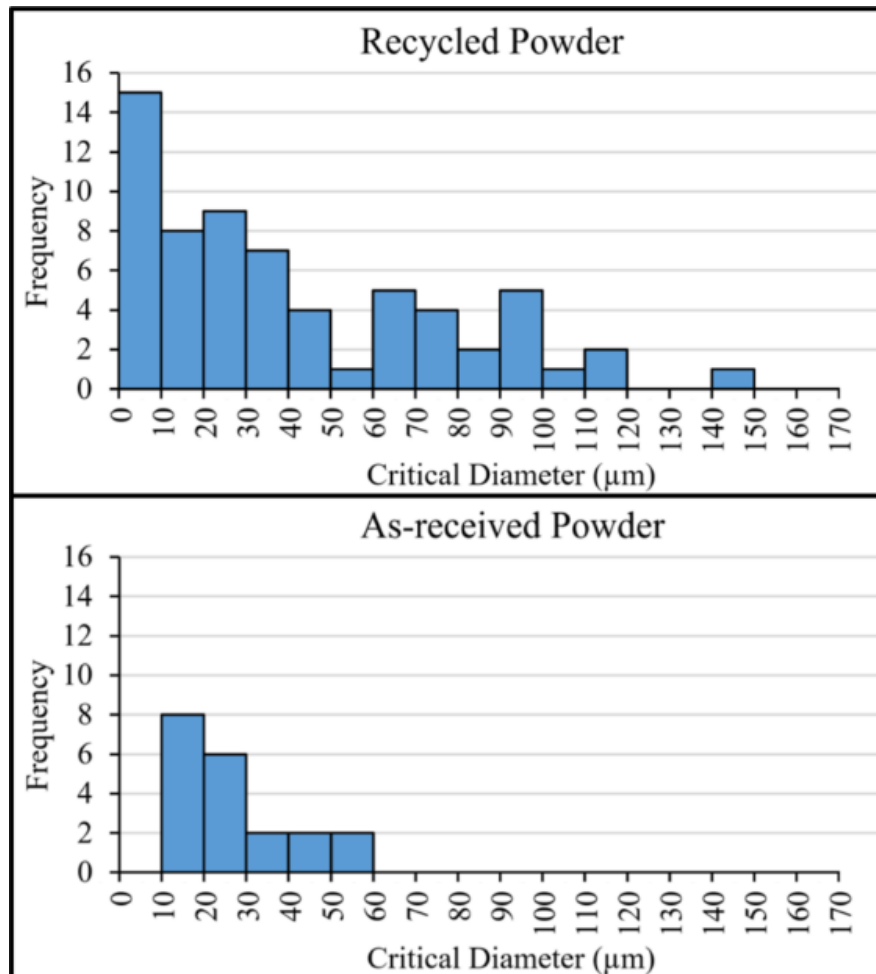
Figure 6-5 Size distribution of porosity found in recycled and as-received powder depositions.

Fig. 6-6 shows the Electron Backscattered Diffraction (EBSD) maps obtained for the as-received powder deposit sample taken from the plane indicated by the sectioning line in Fig. 6-2 and from the top of the rectangle shown in Fig. 6-1. Fig. 6-6a shows that the microstructure was comprised of laths. Fig. 6-6c shows an inverse pole figure with red indicating that the basal plane is parallel to the page. The figure confirms that the crystal orientation was a combination of parallel and Widmanstätten structure. This is in agreement with the optical micrographs presented previously. Fig. 6-6b shows that iron was segregating between the laths. These results were surprising considering that the powder manufacturer measured the iron concentration of the powder to be 780 ppm. The Energy Dispersive X-Ray Spectroscopy (EDS) analysis was not expected to detect iron in such low concentrations. It is possible that some residual iron contaminants in the powder feeder from previous unrelated experiments got introduced to the zirconium powder stream. However, it should also be considered that even with 780 ppm present, these iron atoms will tend to be strongly segregated towards lath boundaries during the solid state transformations in the zirconium. Holt (1970) made a similar observation and noted that α laths grow by edgewise growth and thickening and reject iron in the process. A 2° local subgrain misorientation map revealed that misorientation were concentrating along the lath boundaries. The region inside the laths showed minimal misorientation suggesting that the structure was not deformed. EBSD analysis of recycled powder deposit showed similar results.
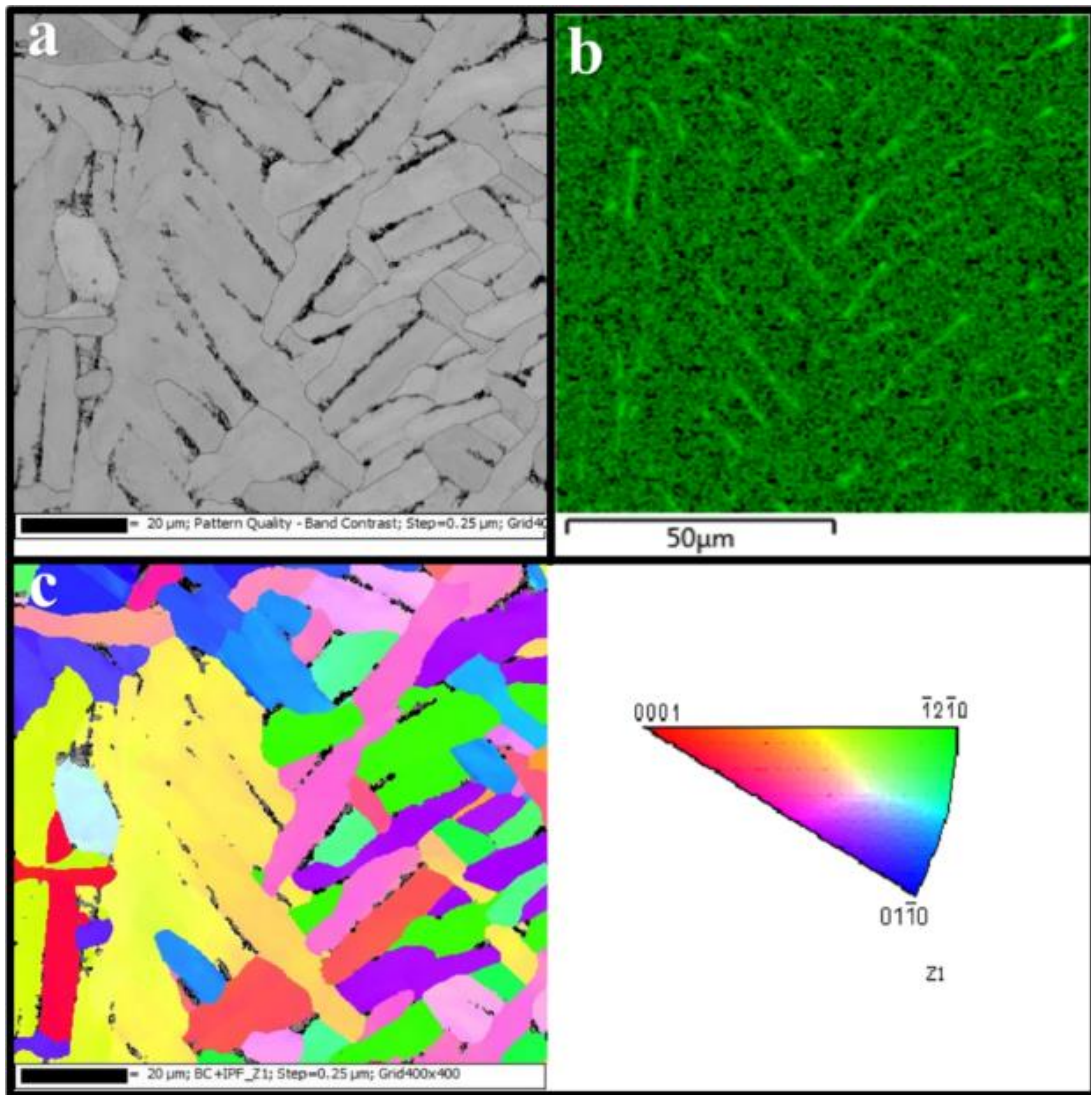
Figure 6-6 EBSD analysis performed on 800 W as-received powder deposition sample that was taken from the top of rectangular box shown in Fig. 6-1 and along the cross sectional lines shown in Fig. 6-2. **a**: microstructure; **b**: EDS map of iron; **c**: inverse pole figure.

TEM analysis was performed on samples that were taken from the plane shown by the sectioning line in Fig. 6-2 and from vertically middle of the rectangle shown in Fig. 6-1. The analysis revealed that the microstructure of both as-received and recycled powder deposits were very similar. As shown by Fig. 6-7a, very fine microstructure was observed originating

from the lath boundary. Surprisingly, EDS analysis revealed that the oval shaped precipitates were made up of iron, nickel, cobalt, copper, chromium and zirconium. Since the total concentration of iron, nickel, cobalt, copper and chromium is expected to be less than ~950 ppm, it is unlikely that these elements came from the original powder batch. It is possible that the zirconium powder got contaminated with previously used powders in the powder feeder, however any contaminants in the initial powder will also tend to get segregated to the lath boundaries. The precipitates were surrounded by a zirconium matrix, and appeared to accumulate at the lath boundary.
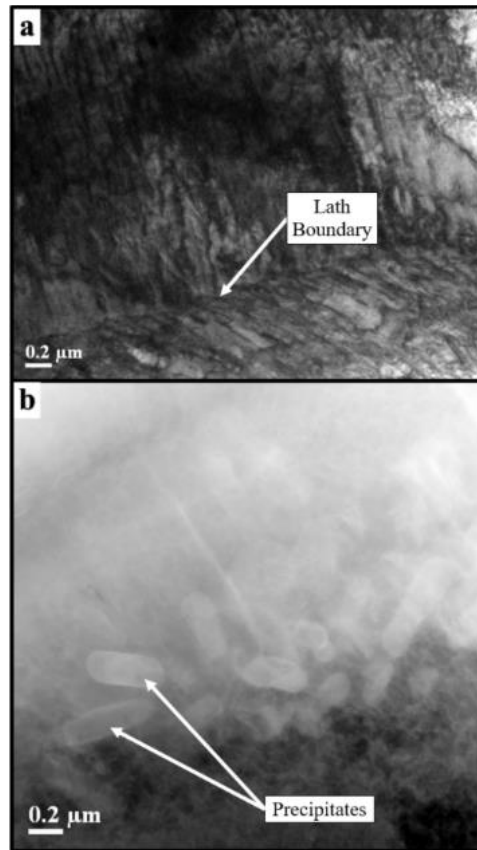
Figure 6-7 TEM of deposition samples taken from vertically middle of rectangular box shown in Fig. 6-1 and along the cross sectional lines shown in Fig. 6-2. **a**: BF microscopy of recycled powder deposition showing microstructure; **b**: HAADF microscopy of as-received powder deposition showing precipitates

6.3 Mechanical Properties

Fig. 6-8 compares the hardness of the 800 W deposits in the build direction to the average hardness of the substrate. Both as-received and recycled powder deposits exhibit a large variation in hardness. Dutta and Froes (2014) noted that during DED LAM of Ti-6Al-4V, the as-deposited microstructure was martensitic. The deposits were then HIP in the α-β region close to β-transus temperature. This caused the microstructure to disintegrate into grain boundary alpha and alpha laths. The formation of martensite is unsurprising because Frazier (2014) reported cooling rates between 10^3 and 10^4 K/s for these kind of systems. It is possible that the variation in hardness in the present study is a result of changes in microstructure and phases. The deposits also showed a general increase in hardness as the distance from the substrate increased. This implies that the earlier layers of deposition were getting tempered by the heat used to deposit the latter layers, which can be expected to occur in terms of the dislocation structure for example. The wide scatter observed between hardness values in adjacent points in Fig. 6-8 was observed to be related to the variability in the grain size in the lath microstructures. This micro-scale variation resulted from the fine indent size used during hardness testing. The lath boundaries around the softer indents were also observed to be more decorated with impurities, suggesting that elemental segregation was having an adverse effect on the mechanical properties of the deposit.

Fig. 6-8 shows a small dip in hardness close to the fusion line. Hardness measurements of single layer clads also showed that adequately shielded clad material was slightly softer than the base material. The softening is attributed to dilution of zirconium with niobium from the base metal and the tempering effect of the laser. As mentioned in Chapter 4, hardness of the deposits was observed to increase with increasing level of atmospheric contamination. Similar increase in hardness can be expected from poorly shielding multi-layer deposits.
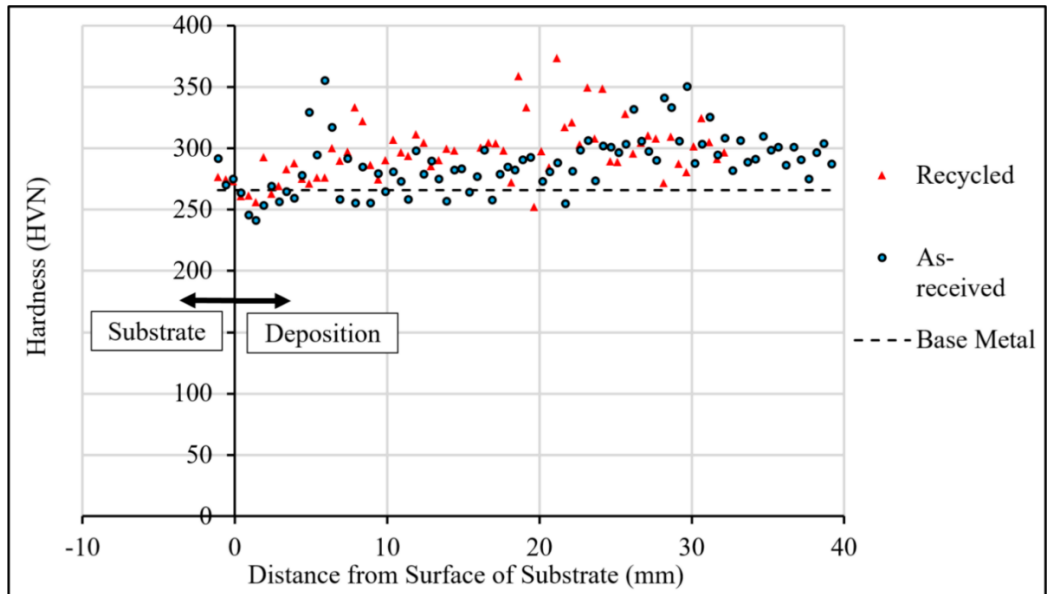
Figure 6-8 Hardness profile of the 800 W recycled and as-received powder deposits

It was difficult to align the deposition during EDM. As shown by Fig. 6-9, this made it hard to get rid of all of the asperities from as-received powder deposit and resulted in a machining defect. During the EDM of recycled powder deposit, misalignment resulted in a groove that was parallel to the cladding direction. After EDM, the as-received and recycled powder deposits were only 1.1 mm thick in the thickness direction. X-ray radiographs of the machined deposits revealed an area of high porosity. This region has been superimposed in Fig. 6-9. The pores were observed to diminish in the build and the cladding direction suggesting that they were eliminated with sufficient preheating. It is expected that this region will diminish with increasing laser power density and interaction time because they will increase the amount of preheating. As shown by Fig. 6-9, the select group of tensile coupon chosen for tensile testing were machined from a region that avoided high porosity and machining defects. Tensile coupons for recycled powder deposition were also machined from similar regions. The labels used to identify these coupons have also been shown in the figure.
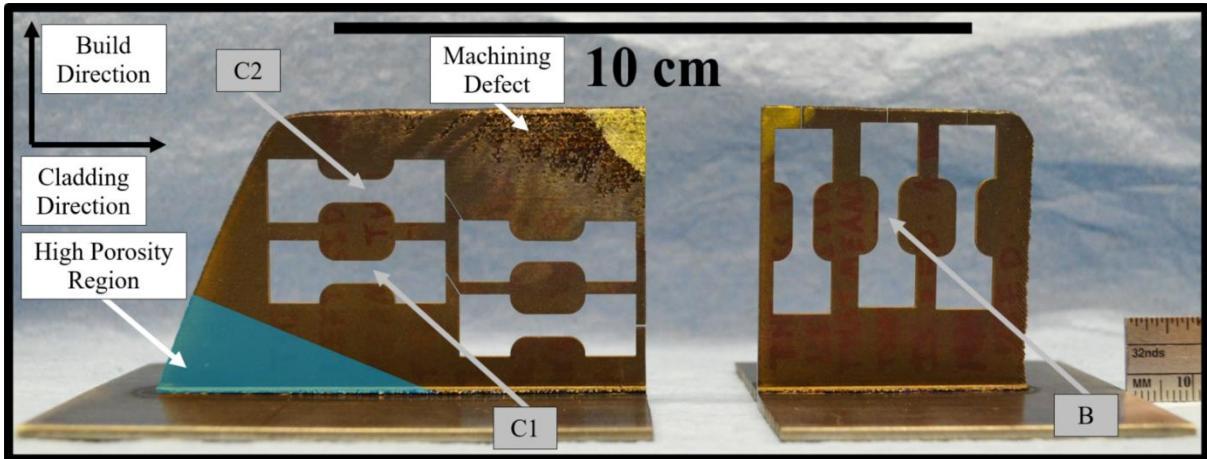
Figure 6-9 As-received powder deposit after EDM. Labels in gray denote the locations from which tensile coupons were extracted.

The tensile properties of recycled and as-received powder deposits have been summarized in Table 6-5. It should be noted that Lustman and Kerze (1955) reported that the Young's modulus of pure zirconium can range from 88.2 GPa to 97.9 GPa. As shown by Fig. 6-10 and Table 6-5, as-received powder "C1" coupon exhibited the highest elongation and the lowest Yield Strength (YS) while the "C2" coupon displayed the lowest elongation and the highest YS. The as-received powder "B" coupon was extracted from the middle of the other two coupons and exhibited medium elongation and YS. The corresponding location of the coupons suggests that the latter cladding layers were tempering the cladding layers deposited earlier. Compared to the as-received powder deposits, the substrate had higher YS. However, the as-received powder deposits had higher UTS and larger UTS/YS ratio.

Although a substrate coupon extracted from a different orientation or exposed to a different thermo-mechanical history will show different tensile properties, the above comparison demonstrates that the zirconium parts made using LAM can have comparable tensile properties to parts manufactured conventionally. Frazier (2014) also found that static properties of Ti-6Al-4V LAM components were quite similar to wrought components. The author also observed slight anisotropy in build direction compared to cladding and thickness directions.

Dutta and Froes (2014) observed that DED LAM Ti-6Al-4V parts that were exposed to a HIP process exhibited slightly lower tensile and yield strength but significantly higher ductility. This suggests that the zirconium deposited during current investigation could benefit from post process heat treatment and/or HIP. Dutta and Froes (2014) also found that Ti-6Al-4V parts produced using LAM had strength and fatigue resistance that was as good or superior than cast, forged or wrought parts.

Fig. 6-10 and Table 6-5 also show that tensile coupons made using recycled powder deposit had much lower ductility. The recycled powder coupons also behaved much more unpredictably and did not always follow the same trend as as-received powder deposit. Since the atmospheric contamination of the recycled and as-received powder deposit was relatively the same, it is believe that the heavily contaminated powder particles were responsible for the poor ductility. These particles are also expected to increase unpredictability by acting as stress risers and contributing to premature failure.
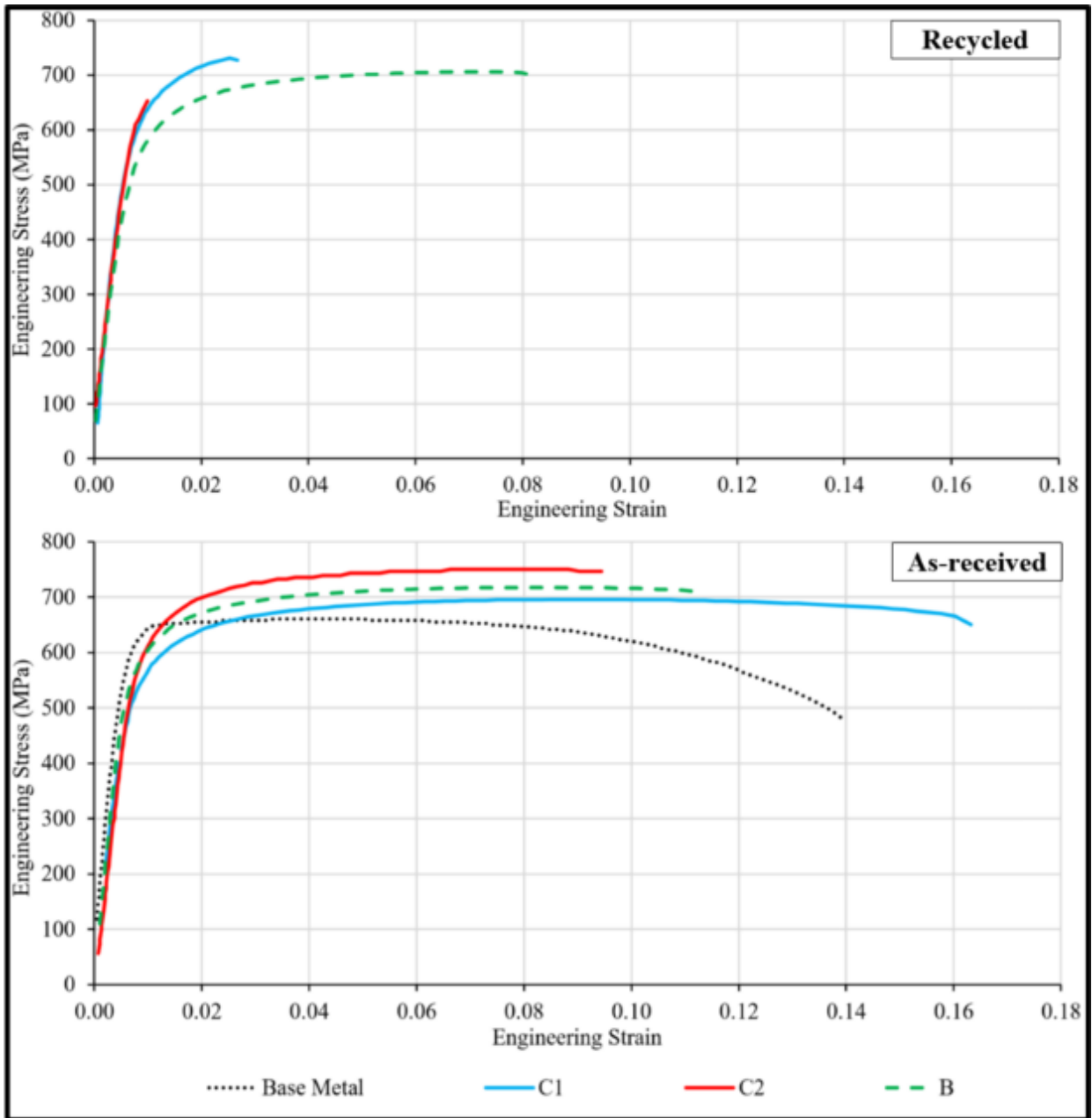
Figure 6-10 Stress vs strain curves of 800 W recycled and as-received powder deposits. The orientation and location of the tensile coupons has been shown in previous image.

Table 6-5 Tensile properties of substrate, 800W recycled and 800W as-received powder deposits

Material	Orientation and/or location	Young's modulus (GPa)	YS (MPa)	UTS (MPa)	Elongation at UTS (MPa)	UTS / YS
Substrate	Rolling	87.3	634	660		1.04
Recycled Powder	C1	93.0	611	731	2.53%	1.19
Recycled Powder	C2	79.0		652	0.993%	
Recycled Powder	B	74.4	573	706	7.54%	1.23
As-received Powder	C1	67.4	569	696	9.90%	1.22
As-received Powder	C2	83.0	590	750	8.82%	1.27
As-received Powder	B	88.8	578	718	8.53%	1.24

The fractured surfaces of the "B" tensile coupons from recycled and as-received powder deposits are compared in Fig. 6-11a and Fig. 6-11b respectively. The recycled powder tensile coupon fracture surface is more faceted and contains a number of pores. This suggests that the pores helped the crack propagate. Fig. 6-11c is a higher magnification image of one such pore and shows a sheared circular powdered particle in the middle of the image. The shearing of the powder particle instead of a pull out suggests that it had been made brittle due to atmospheric contamination. Campbell (2008) mentioned that HCP material with a c/a ratio of less than 1.633 experience improvement in ductility. Lustman and Kerze (1955) reported that pure zirconium has a c/a ratio of 1.593. They also stated that presence of solid solution oxygen increases the c/a ratio and makes the crystal structure less closely packed. This would adversely affect zirconium's ductility by reducing the number of slip systems available to it. It is very likely that the sheared powder particle was heavily contaminated by oxygen. Since oxygen (Abriata et al., 1986) and nitrogen (Gribaudo et al., 1994) increase the melting point of zirconium, their presence is expected to increase the level of undercooling required and delay the solidification process. The crescent shaped porosity immediately to the left of the powder

particle was likely formed when the molten metal adjacent to the powder particle solidified before it could completely surround the particle. It is also likely that the roughly circular region immediately above the powder particle had been contaminated from the adjacent powder particle and consequently also failed in a brittle manner. There were also instances when powder particles pulled out instead of shearing, suggesting that these particles were not as contaminated with oxygen and nitrogen as the one shown in Fig. 6-11c. The pull-out of the powder particle shows that its interface was not as strong as the surrounding material. This was likely due to increased concentration of oxygen and nitrogen around the particle that would promote lack of fusion by increasing melting point. It would also make the rest of the interface more brittle by increasing the HCP crystal c/a ratio. It appears that failure initiated around these contaminated powder particles that had cavities and brittle regions around them.

Fig. 6-11d is a higher magnification image of the fracture surface of the as-received powder deposit shown in Fig. 6-11b. The image shows intergranular failure with crack following lath boundaries. The fracture surface of recycled powder deposit away from the pores looked similar to Fig. 6-11d.
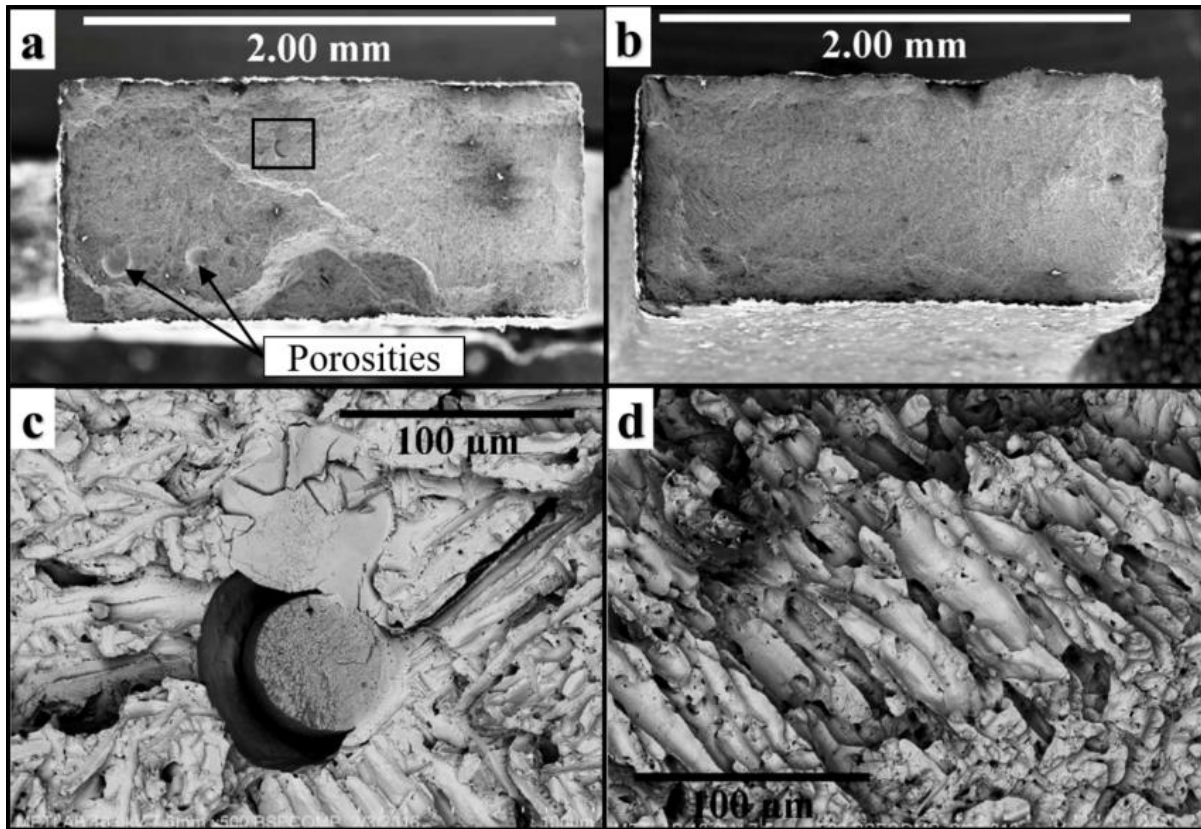
Figure 6-11 SEM of the fractured 800 W "B" tensile coupons. **a**: recycled powder deposit; **b**: as-received powder deposit; **c**: higher magnification image of the rectangle shown in **a**; **d**: higher magnification image of the fractured surface from **b**.

Chapter 7– Conclusion[**]

1. This work not only proves that laser cladding and LAM of zirconium is possible but also that it can be done with only localized shielding using a modified TIG nozzle instead of an enclosed inert gas environment. This work is significant because very little research has been done on depositing zirconium on a zirconium based substrate and can allow in-situ repair of components made out of zirconium or other reactive metals.

2. Although a higher level of atmospheric contamination was observed in LAM deposits made using localized shielding, the present work shows that these levels can be reduced with a properly designed shielding apparatus. It was found that atmospheric contamination levels comparable to conventionally manufactured parts can be achieved.

3. Increasing the interaction time and preheating reduced the level of porosity in the resultant clads.

4. Higher deposition rates can be achieved by preheating the powder stream.

5. Iron, nickel, cobalt, copper and chromium elemental impurities were observed to segregate to lath boundaries suggesting that LAM technology might be unsuitable for high alloy content zirconium alloys.

6. With the exception of larger and more numerous pores in recycled powder, the microstructure of as-received and recycled powder deposits was very similar. Most of the porosity appear to be an artifact of a small percentage of powder particles that were highly contaminated with atmospheric gases. Although the contaminated particles decrease ductility by acting as crack initiators, they were not able to change the overall chemical composition of the bulk material.

[**] Parts of this section were published in a non-peer reviewed conference paper entitled "Comparison of Nozzle Gas Shielding Techniques for Laser Cladding of Zirconium" at International Congress on Applications of Lasers & Electro-Optics (ICALEO®). Parts of this section were also published in a paper entitled "Processing Window Development for Laser Cladding of Zirconium on Zirconium Alloy" in Journal of Materials Processing Technology

7. Since tempering from latter clads layers was observed to improve the ductility of previous clad layers, it is believed that the present deposits might benefit from HIP or post process heat treatment.

8. As-received powder deposit had tensile properties comparable to conventionally manufactured zirconium alloy substrate.

Chapter 8 – Future Work

A number of paths can be taken to further this research. Although Chapter 5 showed clear trends by varying various process parameters, picking fewer parameters and conducting a more controlled experiment will allow statistically strong conclusions to be drawn. Further process optimization will result in deposits with better geometries and properties. A more detailed analysis on size and spacing between cavities may help explain fracture behaviour. Building larger tensile coupons will allow the DIC system to calculate the Lankford Coefficient (R-value). This will allow characterization of the plastic anisotropy of the material. Studying the influence of post process HIP and heat treatment would also be of great interest. This research can be expanded to develop new zirconium based materials and composite. The high glass forming ability of zirconium makes this particular area of research especially exciting (Wu and Hong, 2000). Another area of research could be application of pure zirconium cladding on existing materials to impart desirable properties.

Studying the influence of distance from the powder delivery nozzle to the deposition will have a great impact on process optimization. Although decreasing this distance increases the amount of powder and shielding gas reaching the melt pool, it also increases the chances of the nozzle getting damaged during the deposition. The nozzle fixture will need to be modified to allow better control over this distance. Further improvement in inert gas shielding is expected to create depositions that are acceptable according to AWS (2012) standards. Trailing gas shielding can be added to improve the shielding. Additional shielding gas supply can be used to improve the projection area and shielding density. Addition of a coaxial powder delivery and shielding gas nozzle will improve the processing time by allowing the LAM system to create deposition in more than one direction. An optimization study on the amount of overlap necessary between two clads deposited side by side will allow the system to make thicker walled geometries. Adding additional preheating to the substrate and/or the powder is expected to reduce porosity, increase deposition rate and diminish the amount of laser power necessary to create a continuous and adherent deposits. Adding a laser power or laser scan

speed ramp up function at the beginning of a clad layer will improve the profile of the overall deposit. Finally, remelting or laser heat treating a clad layer that has just been deposited can improve geometry and tensile properties of the overall deposit.

As zirconium and its alloys react readily with atmospheric gases at high temperatures (Bláhová et al., 2009), complex manufacturing is required to process them. The advent of LAM can expedite the process of creating new zirconium alloys by allowing material scientists and engineers to build parts in the geometry necessary for evaluating the new alloy. Due to the high glass forming ability of zirconium and high cooling rates created by the laser (Wu and Hong, 2000), it might be possible to create complex 3D parts out of metallic glass. This would be especially advantageous because forming and material processing of metallic glass is challenging. LAM can also offer an easier method of creating zirconium MMC. LAM can also allow creation of functionally grade zirconium alloy and/or MMC parts which is not possible with conventional manufacturing processes. This may be easily done by mixing the feed zirconium powder stream with other particles such as alumina or carbides for example.

The findings in this thesis can also be useful for the development of zirconium based coatings on non-zirconium substrates. For example, deposition onto a stainless substrate may provide a compromise between a coating with good corrosion properties while reducing cost of the component. However, it is vital that cracking is suppressed in the deposit, since many intermetallics may form when depositing zirconium onto steels.

Bibliography

1   Abriata, J., Garces, J., Versaci, R., 1986. The O− Zr (Oxygen-Zirconium) system. Bulletin of Alloy Phase Diagrams 7, 116-124.

2   Arora, H.S., Grewal, H.S., Singh, H., Dhindaw, B.K., Mukherjee, S., 2013. Unusually high erosion resistance of zirconium-based bulk metallic glass. Journal of Materials Research 28, 3185-3189.

3   AWS, 2012. American Welding Society G2.5/G2.5M:2012 Guide for the Fusion Welding of Zirconium and Zirconium Alloys.

4   Balla, V.K., Xue, W., Bose, S., Bandyopadhyay, A., 2009. Laser-assisted Zr/ZrO 2 coating on Ti for load-bearing implants. Acta biomaterialia 5, 2800-2809.

5   Baloyi, N., Popoola, A., Pityana, S., 2014. Laser coating of zirconium and ZrO2 composites on Ti6Al4V for biomedical applications. South African Journal of Industrial Engineering 25, 62-70.

6   Bhadeshia, H.K.D.H., 2011. Titanium and its Alloys, In: Bhadeshia, H.K.D.H. (Ed.), Metals & Alloys (year 3). Youtube, p. 42:52.

7   Bláhová, O., Medlín, R., Ríha, J., 2009. Evaluation of Microstructure and Local Mechanical Properties of Zirconium Alloys, Conference proceeding Metal, pp. 359-365.

8   Brachet, J.C., Toffolon-Masclet, C., Hamon, D., Guilbert, T., Trego, G., Jourdan, J., Stern, A., Raepsaet, C., 2011. Oxygen, Hydrogen and Main Alloying Chemical Elements Partitioning Upon Alpha←→ Beta Phase Transformation in Zirconium Alloys, Solid State Phenomena. Trans Tech Publ, pp. 753-759.

9   Campbell, F.C., 2008. Elements of metallurgy and engineering alloys. ASM International.

10 Carroll, B.E., Palmer, T.A., Beese, A.M., 2015. Anisotropic tensile behavior of Ti–6Al–4V components fabricated with directed energy deposition additive manufacturing. Acta Materialia 87, 309-320.

11 Courtois, M., Carin, M., Le Masson, P., Gaied, S., Balabane, M., 2013. A new approach to compute multi-reflections of laser beam in a keyhole for heat transfer and fluid flow modelling in laser welding. Journal of Physics D: Applied Physics 46, 505305.

12 Danielson, P.E., Sutherlin, R.C., Chang, W., 2004. Metallography and microstructures of zirconium, hafnium, and their alloys. Materials Park, OH: ASM International, 2004., 942-958.

13 Dutta, B., Froes, F., 2014. Additive Manufacturing of Titanium Alloys. Advanced Materials & Processes 172, 18-23.

14 Emamian, A., 2011. In-Situ TiC-Fe Deposition on Mild Steel Using a Laser Cladding Process.

15 EOS, 2014. EOS in Brief. EOS.

16 Ferreira, T., Rasb, W., 2012. ImageJ user guide.

17 Fraunhofer IWS, 2011. Laser Cladding. Fraunhofer IWS.

18 Frazier, W.E., 2014. Metal additive manufacturing: A review. Journal of Materials Engineering and Performance 23, 1917-1928.

19 Gribaudo, L., Arias, D., Abriata, J., 1994. The N-Zr (nitrogen-zirconium) system. Journal of phase equilibria 15, 441-449.

20 Harooni, A., Gerlich, A.P., Khajepour, A., Khalifa, A., King, J.M., 2015. Comparison of Nozzle Gas Shielding Techniques for Laser Cladding of Zirconium, The International Congress on Applications of Lasers & Electro-Optics. ASM international, Atlanta, Ga, pp. 404-409.

21 Harooni, A., Nasiri, A.M., Gerlich, A.P., Khajepour, A., Khalifa, A., King, J.M., 2016. Processing window development for laser cladding of zirconium on zirconium alloy. Journal of Materials Processing Technology 230, 263-271.

22 Holt, R., 1970. The beta to alpha phase transformation in Zircaloy-4. Journal of Nuclear Materials 35, 322-334.

23 Johnson, D., Orakwe, P., Weckman, E., 2006. Experimental examination of welding nozzle jet flow at cold flow conditions. Science and Technology of Welding and Joining 11, 681-687.

24 Joining Technologies, 2011. Laser Cladding Company Video. Joining Technologies, Inc.

25 Klar, E., Samal, P.K., 2007. Powder metallurgy stainless steels: processing, microstructures, and properties. ASM international.

26 Li, C., Li, J., Wang, W., Tani, K., 1998. Thermal Spray: Meeting the Challenges of the 21st Century, Proc. of 15th International Thermal Spray Conference, pp. 287-292.

27 Lumex Avance-25, 2014. Metal Laser Sintering Hybrid Milling Machine. Mitsubishi Corporation.

28 Lustman, B., Kerze, F., 1955. The metallurgy of zirconium. McGraw-Hill Book Company.

29 Matsunawa, A., Katayama, S., Kohsaka, S., Mizutani, M., Nishizawa, K., 1994. Pulse Shape Optimization for Defect Prevention in Pulsed Laser Welding of Stainless Steels, Laser Materials Processing, p. 487.

30 Meng, W., Li, Z., Huang, J., Wu, Y., Cao, R., 2013. Effect of gap on plasma and molten pool dynamics during laser lap welding for T-joints. The International Journal of Advanced Manufacturing Technology 69, 1105-1112.

31 Monfared, A., Vali, H., Faghihi, S., 2013. Biocorrosion and biocompatibility of Zr–Cu–Fe–Al bulk metallic glasses. Surface and Interface Analysis 45, 1714-1720.

32 NFPA, 1996. National Fire Protection Association 482, Standard for the Production, Processing, Handling and Storage of Zirconium. National Fire Protection Association.

33 Nikulina, A.V., Malgin, A.G., 2008. Impurities and Their Effect on Structure and Properties of Zirconium Parts in Nuclear Reactors. Atomic energy 105, 328-339.

34 Optomec, 2014. Core Applications. Optomec.

35 Read, N., Wang, W., Essa, K., Attallah, M.M., 2015. Selective laser melting of AlSi10Mg alloy: Process optimisation and mechanical properties development. Materials & Design 65, 417-424.

36 Renishaw Canada, 2014. Innovation Applied. Renishaw.

37 Sattari, M., Holt, R., Daymond, M., 2013. Phase transformation temperatures of Zr alloy Excel. Journal of Nuclear Materials 435, 241-249.

38 Sciaky, I., 2015. Advantages of Wire AM vs. Powder AM. Sciaky Inc.

39 Siewert, E., Wilhelm, G., Häßler, M., Schein, J., Hanson, T., Schnick, M., Füssel, U., 2014. Visualization of gas flows in welding arcs by the schlieren measuring technique. Weld. J 94, 1s-5s.

40 SLM Solutions NA, I., 2014. Laser Beam Melting System SLM. SLM solutions.

41 Steen, W., Watkins, K.G., Mazumder, J., 2010. Laser material processing. Springer Science & Business Media.

42 Tewari, R., Srivastava, D., Dey, G., Chakravarty, J., Banerjee, S., 2008. Microstructural evolution in zirconium based alloys. Journal of Nuclear Materials 383, 153-171.

43 Toyserkani, E., Khajepour, A., Corbin, S.F., 2004. Laser cladding. CRC press.

44 Weldcraft, 2016. Top five tips for improving your TIG welding efficiency. Plant Services.

45 Wright, M., 2015. Zr Deposition Update, In: Gerlich, A.P., King, J.M., Khalifa, A., Wright, M., St Lawrence, S. (Eds.). University of Waterloo, Waterloo, ON.

46 Wu, X., Hong, Y., 2000. Microstructure of Zr-alloyed coating using pulsed laser. Surface and Coatings Technology 132, 194-197.

47 Yue, T., Xie, H., Lin, X., Yang, H., 2012. Microstructure development in laser forming of zirconium coatings on AZ91D magnesium alloy substrates. Journal of Alloys and Compounds 512, 328-331.

48 Zhou, J., Tsai, H.-L., 2007. Porosity formation and prevention in pulsed laser welding. Journal of Heat Transfer 129, 1014-1024.

49 Zschetzsche, I.J., 2012. Visualization and optimization of shielding gas flows in arc welding. Welding in the World 56, 54-61.

Appendix A

Table A 1 Prices and build chamber volume of popular SLS and LDMD systems (EOS, 2014; Optomec, 2014; Renishaw Canada, 2014; SLM Solutions NA, 2014)

Manufacturer	SLM Solutions	SLM Solutions	Renishaw	EOS	Optomec	Optomec
Model	SLM 125	SLM 500	AM 250	EOS M 290	LENS 450	LENS MR-7
System Type	SLS	SLS	SLS	SLS	LPMD	LPMD
Build Chamber Volume [x/y/z] in mm	125 x 125 x 75	500 x 280 x 320	245 x 254 x 300	250 x 250 x 325	100 x 100 x 100	300 x 300 x 300
Price (in thousands of CAD)	$400	$1 200	$650	$700	$400	$850

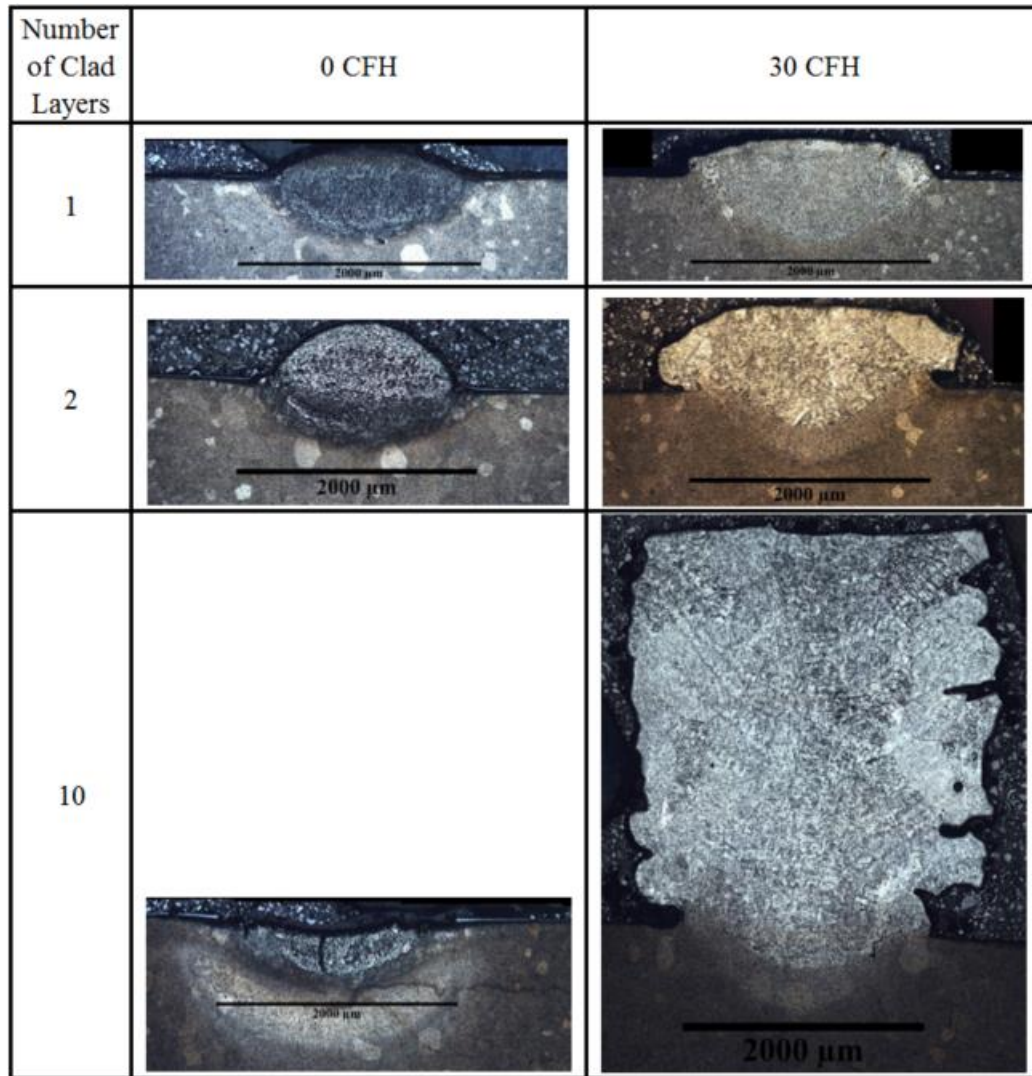| Number of Clad Layers	0 CFH	30 CFH
1		
2		
10		

Figure A 1 Effect of auxiliary shielding gas flow rate on cross-section of multi layered clads. The parameters used were: Laser spot diameter = 1.4mm; Laser power = 800W; Laser scan speed = 123mm/min; Powder feed rate = 4.0g/min; Powder condition = as-received; Auxiliary shielding gas nozzle type = TIG; Nozzle inner diameter = 15.9mm

Glossary

3D	Three Dimensional
$\hat{A}$	Projection area
AM	Additive Manufacturing
BCC	Body Centered Cubic
BF	Bright Field
CNC	Computerized Numerical Controlled
DED	Direct Energy Deposition
DIC	Digital Image Correlation
EBSD	Electron Backscatter Diffraction
EDM	Electrical Discharge Machining
EDS	Energy Dispersive X-Ray Spectroscopy
FZ	Fusion Zone
HAADF	High Angle Annular Dark Field
HAZ	Heat Affected Zone
HCP	Hexagonal Closed Packed
HIP	Hot Isostatic Pressing
ICP Spectroscopy	Inductively Coupled Plasma Spectroscopy
ID	Inner Diameter
LAM	Laser Additive Manufacturing
MIG	Metal Inert Gas
MMC	Metal Matrix Composite
PBF	Powder Bed Fusion
ppm	parts per million
TEM	Transmission Electron Micrograph
TIG	Tungsten Inert Gas
S	Shielding density

SEM	Scanning Electron Micrograph
UTS	Ultimate Tensile Strength
YS	Yield Strength